Shallow Tectonic Stress Magnitudes at the Hikurangi Subduction Margin, New Zealand

E. Behboudi[1,2], D.D. McNamara[3], I. Lokmer[1,2]

[1] Irish Centre for Applied Geosciences (iCRAG), University College Dublin, Republic of Ireland.

[2] School of Earth Sciences, University College Dublin, Republic of Ireland.

[3] Department of Earth, Ocean and Ecological Sciences, University of Liverpool, UK.

Corresponding author: Effat Behboudi (effat.behboudi@ucdconnect.ie)

Abstract

Quantifying tectonic stress magnitudes is crucial in understanding crustal deformation processes, fault geomechanics, and variable plate interface slip behaviors in subduction zones. The Hikurangi Subduction Margin (HSM), New Zealand is characterized by along-strike variation in interface slip behavior, which may be linked to tectonic stress variations within the overriding plate. This study constrains *in-situ* stress magnitudes of the shallow (<3km) overriding plate of the HSM to better understand its tectonics and how they relate to larger scale subduction dynamics. Results reveal σ_3: S_v ratios of 0.6-1 at depths above 650-700 m TVD and 0.92-1 below this depth interval along the HSM and S_{Hmax}: S_v ratios of 0.95-1.81 in the central HSM, and 0.95-3.12 in the southern HSM. These stress ratios suggest a prevalent thrust to strike-slip (σ_1=S_{Hmax}) faulting regime across the central and southern HSM. In the central HSM, the presence of NNE-NE striking reverse faults co-existing with a modern σ_1 aligned ENE-WSW (S_{Hmax}) suggests that overtime the stress state here evolved from a contractional to a strike-slip state, where the compressional direction changes from perpendicular (NW-SE) to subparallel (ENE-WSW) to the Hikurangi margin. This temporal change in stress state may be explained by forearc rotation, likely combined with development of upper plate overpressures. In the southern HSM, the modern WNW-ESE/ NW-SE σ_1 (S_{Hmax}) and pre-existing NNE-NE striking reverse faults indicate that stress state remains contractional and subparallel (NW-SE) to the Hikurangi margin overtime. This may reflect the interseismic locked nature of the plate interface.

Plain Language Summary

The type of geological faults and their movement are partially controlled by forces generated from plate movement, known as in-situ stress. This stress state can also be changed overtime due to the occurrence of earthquakes on such faults. The HSM is New Zealand's largest and most hazardous plate boundary fault and experiences different types of earthquakes that may be related to variations in in-situ stress of the plates involved in this subduction boundary. This study quantifies for the first time the stresses associated with the modern HSM, and finds that they and their resulting tectonic behavior have changed with geological time in the central regions. This change is likely related to the effects of other nearby tectonic processes further inland and to the development of high pore pressures in the overriding plate in this region.

Key Points

- For the shallow crust (upper 3 km) of the Hikurangi Subduction Margin, $\sigma_1 = S_{Hmax}$.
- σ_1 rotates from margin-parallel (NW-SE) to margin-perpendicular (WNW-ESE) in the central Hikurangi Subduction Margin overtime.
- The shift in the stress state overtime in the central HSM may be driven by forearc rotation and shallow overpressures in this region.
- σ_1 remains perpendicular (NW-SE/WNW-ESE) to the margin overtime in the southern HSM, may reflect the interseismic locked nature of the plate interface.

1 Introduction

Large magnitude, tsunamigenic earthquakes commonly occur at subduction plate boundaries and are associated with a wide range of tectonic fault slip behaviors along the subduction interface including slow slip events (SSEs), low-frequency earthquakes (LFEs), very-low-frequency earthquakes (VLFEs), and episodic tremor and slip (ETS) (Audet et al., 2009; Ito & Obara, 2006; Kodaira et al., 2004; Liu & Rice, 2007; Ujiie & Kimura, 2014). Earthquake occurrence such as nucleation of earthquake ruptures and rupture propagations, and a variety of seismic slip behaviors are, in part, controlled by the interaction between *in-situ* stresses (their orientations and magnitudes), the mechanical and geometrical properties of crustal faults, and pore pressure (Jaeger et al., 2009; Schellart & Rawlinson, 2013; Vavrycuk, 2015). Furthermore, seismic cycling and slip on faults are known to drive temporal changes in the stress state on adjacent fault planes and surrounding rocks (Brodsky et al., 2017, 2020; Hardebeck & Okada, 2018; K. F. Ma et al., 2005; Seeber & Armbruster, 2000; Stein, 1999). For example, significant principal stress rotations followed the 2011 M_w 9.0 Tohoku earthquake in Japan, 2010 M_w 8.8 Maule earthquake in Chile; and 2004 M_w 9.2 earthquake in Sumatra-Andaman are suggested to be related to near-complete stress drops (Hardebeck, 2012). Therefore, quantitative knowledge of stress is an essential step to characterize and understand the nature and causes of earthquake processes, the mechanical behavior of plate boundary faults, the origin and controls of diverse fault slip patterns; and to better assess seismic and tsunamigenic hazards along subduction zones (Huffman & Saffer, 2016; Riedel et al., 2016; Wu et al., 2019).

The Hikurangi Subduction Margin (HSM), New Zealand displays along-strike variation in plate interface slip behavior, ranging from episodic SSEs and creep at the northern and

central HSM, to deep interseismic locking beneath the southern North Island (Wallace & Beavan, 2010) (Figure 1a). Creep and shallow (<15 km depth) SSEs, lasting for 2–3 weeks, recur every 1 to 2 years offshore the northern and central HSM (Wallace, Beavan, et al., 2012) (Figure 1a). Deep (>25 km), long-term (>1 year) SSEs occur approximately every ~5 years at the southern HSM (Wallace & Beavan, 2010), down-dip from a portion of the plate interface that is locked and accumulating stress (Wallace et al., 2009). The physical processes controlling SSEs are currently debated, with studies suggesting they are linked to the frictional properties of fault zone materials (e.g., strength and coefficient of friction), low effective stress linked to high pore pressure, fault heterogeneity, and fault rheology (Ando et al., 2012; Kodaira et al., 2004; Kurzawski et al., 2018; Saffer & Wallace, 2015). More than 80% of HSM historic earthquakes and $M_w \geq 6$ earthquakes occur on upper plate ($\leq$30 km) faults or at the plate interface (Figure 1a) (Doser & Webb, 2003; Downes, 2006; Grapes & Downes, 1997; Webb & Anderson, 1998). Earthquakes located within the subducting slab or at the plate interface have also been known to trigger slope failures or series of smaller earthquakes hosted on upper plate faults, some of which can be tsunamigenic (Beetham et al., 2018; Lange & Moon, 2004; Power et al., 2008).

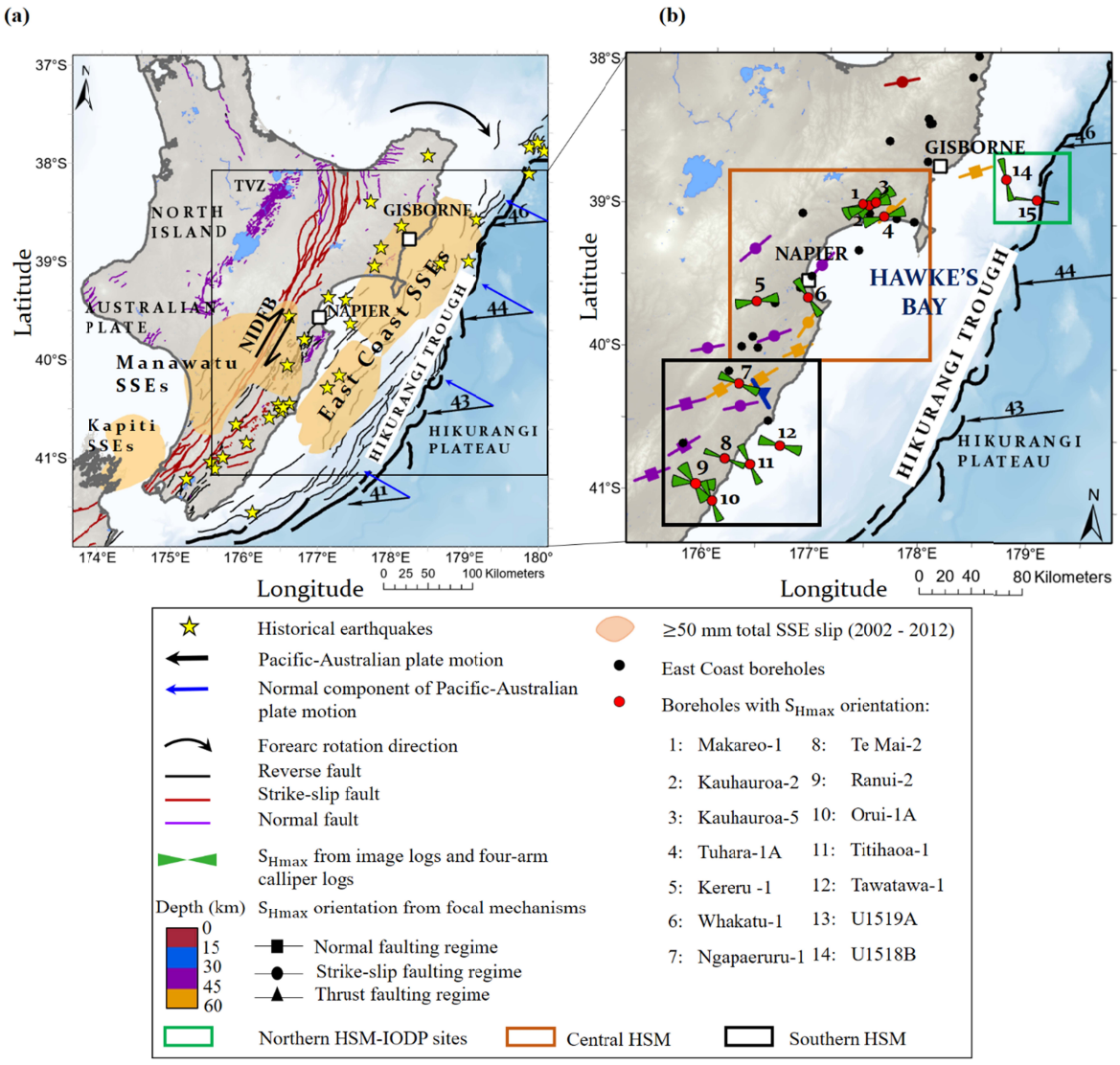

Figure 1. (a) Map of the tectonic structures and regions that have experienced cumulative slow slip of ≥50 mm between 2002 and 2012 in North Island, New Zealand (Wallace & Eberhart-Phillips, 2013). Fault traces from Barnes et al. (2010), Langridge et al. (2016), Mountjoy and Barnes (2011), and Pedley et al. (Pedley et al., 2010). Yellow stars are historic earthquakes (Doser & Webb, 2003; Downes, 2006; Grapes & Downes, 1997; Webb & Anderson, 1998) and $M_w \geq 6$ earthquakes from August 2000 to 2022 (https://www.geonet.org.nz/). Black arrows indicate long-term relative motion between Pacific and Australian plates (Beavan et al., 2002). Blue arrows show motion of the Pacific Plate relative to overriding plate (or normal component of Pacific-Australian plate motion). (b) Map showing borehole-derived S_{Hmax} orientations (Behboudi et al., 2022; Mcnamara et al., 2021), and focal mechanisms derived S_{Hmax} orientations (Townend et al., 2012). Abbreviations: NIDFB = North Island Dextral Fault Belt; TVZ = Taupo Volcanic Zone.

Shallow horizontal stress orientations within the HSM have recently been constrained via borehole data analyses (Behboudi et al., 2022; Griffin, 2019; Griffin et al., 2021; Heidbach et

al., 2018; Lawrence, 2018; McNamara et al., 2021). Behboudi et al. (2022) provides a comprehensive overview of the along-strike and depth related variability in HSM stress orientations. Borehole-derived S_{Hmax} orientations rotate from ENE-WSW (065°/245° ± 10°) in the central HSM to WNW- ESE (112°/292° ± 20°) and NW- SE (140°/320° ± 22°) in the southern HSM (Figure 1b). Deep stress orientations are defined by focal mechanism inversions (Townend et al., 2012), shear wave anisotropy (Illsley-Kemp et al., 2019), and gravitational stresses (Evanzia et al., 2017). Earthquake focal mechanism solutions (≤60 km depth) indicate a regional S_{Hmax} orientation of 060°/240° ± 17° and 066°/246° ± 22° in the central and southern HSM, respectively (Figure 1b) (Behboudi et al., 2022; Townend et al., 2012).

The characterization of stress magnitudes at the HSM are currently limited to relative stress magnitudes derived from earthquake focal mechanisms at seismogenic depths (Townend et al., 2012), and direct measurements of the minimum principal stress magnitudes (σ_3), vertical stress magnitudes (S_v), pore pressures (P_p) at shallow depths (< 3km) (Burgreen-Chan et al., 2016; D. Darby & Ellis, 2001; D. Darby & Funnell, 2001), and stress regime in one borehole (Tuhara-1A) in the central HSM (HRT, 2000). Observations of relative stress magnitudes (≤60 km) by Townend et al. (2012) indicate a predominantly strike-slip and normal faulting regime along the HSM. P_p measured from repeat formation tests (RFTs) and modular dynamic tests (MDTs), and inferred from drilling mud weights reveal shallow (<3 km) overpressures within the upper plate of the central HSM (Burgreen-Chan et al., 2016; D. Darby & Funnell, 2001). High pore pressure in central and northern HSM are attributed to disequilibrium compaction of Miocene sediments and porosity reduction due to high horizontal compressive stresses associated with subduction of Hikurangi Plateau beneath the continental crust of North Island, New Zealand (Burgreen-Chan et al., 2016; David Darby & Funnell, 2001). σ_3 magnitudes determined from leak-off tests are less than or close to S_v magnitudes (Burgreen-Chan et al., 2016), suggesting variable normal, strike-slip, and a reverse faulting regimes along the HSM.

In this study, we apply an indirect approach to constrain the three principal stress magnitudes along the shallow HSM crust using openly available borehole data. We discuss our findings in the context of understanding the upper plate tectonics within the HSM forearc. This study, in combination with stress orientation studies already completed for the HSM, provides a deeper insight into the variable tectonic behaviors associated with subduction margins, and will serve as crucial information to assist in future hazard assessments of this region.

2 Geologic setting and background

The HSM at the east coast of North Island, New Zealand is a site of recent significant scientific investigation into the complexity of subduction dynamics. The HSM is formed by westward subduction of the oceanic crust of the Hikurangi Plateau beneath the continental crust of the North Island of New Zealand (Davy, 1992; Davy et al., 2008). The oblique relative motion of the Australian-Pacific plate increases from ~31 mm/year in the southern to ~48 mm/year in the northern North Island (Figure 1a) (Wallace et al., 2004). Tectonic deformation across the HSM ranges from subduction-related shortening at the Hikurangi Trough, strike-slip faulting along the North Island Dextral Fault Belt (NIDFB), and back-arc extensional tectonics in the Taupo Volcanic Zone (TVZ) at the center of North Island (Wallace et al., 2004; Figure 1a). The East Coast forearc has rotated at rate of 3°–4°/Myr relative to the Australian plate, resulting in the TVZ back-arc rifting, strike-slip and/or normal faulting in the onshore portion of the northern and central HSM, transpressional faulting in the southern HSM, and a large along-strike variation in convergence rate at the Hikurangi Trough (Figure 1a) (Fagereng & Ellis, 2009; Nicol et al., 2007; Wallace et al., 2004; Wallace, Fagereng, et al., 2012). The oblique motion of the Australian-Pacific plate is partitioned into a margin-perpendicular component and a margin-parallel component. The margin-perpendicular component occurs along the Hikurangi subduction interface and provides NW-SE shortening mostly accommodated by slip on the subduction interface (>80%) and active frontal thrusts in the overriding plate (Nicol & Beavan, 2003). The margin-parallel component is largely accommodated by a combination of right-lateral strike-slip on the North Island Dextral Fault Belt (NIDFB) and clockwise rotation of the North Island forearc (Beanland & Haines, 1998; Nicol et al., 2007; Wallace et al., 2004).

3 Methodology and Data

3.1 Data Sources and Limits

Data used in this study is sourced from 44 boreholes along the HSM (Figure 1), 41 of them are located within the onshore forearc and 3 are located offshore the east coast of NZ but west of the Hikurangi Trough. Data utilised includes wireline logging acquired over the period 1967-2013 from 0 to a maximum depth of 4350 m below ground level. Wireline data includes density logs from 26 boreholes, sonic velocity logs from 24 boreholes, and borehole image logs from 10 boreholes. Data presented here include the analysis of 21 leak-off tests and 39 formation integrity tests from 30 boreholes spanning a depth range of 3 71.5 to 3610.6

m, mud weight logs from 44 boreholes, and repeat formation test results from 2 boreholes spanning a depth range of 1335-2700 m. How each of these data are utilised in determining aspects of the in situ-stress magnitudes across the HSM is detailed below. All depths in this study is referenced to ground level for onshore boreholes and sea level for offshore boreholes.

3.2 Vertical stress magnitude (S_v)

Assuming the vertical stress (S_v) is aligned to one of the principal stresses, the S_v magnitude at any specific subsurface depth can be determined by the integration of rock densities from the surface to the depth of interest (equation 1):

$$S_V = \rho_w g Z_w + \int_{Z_w}^{Z} \rho(Z)\, g\, dZ \approx \rho_w g Z_w + \bar{\rho} g (Z - Z_w) \quad (1)$$

where ρ_w is the average seawater density (1.03 g/cm^3), g is the gravitational acceleration constant (~ 9.81 m/s^2), Z_w is the depth of the water column (m), Z is the depth of interest (m), $\rho(Z)$ (g/cm^3) is bulk density of the rock as a function of depth, and $\bar{\rho}$ (g/cm3) is the average density of the rock column above Z. For onshore boreholes, Z_w is equal to zero.

We utilise 26 density wireline logs to estimate S_v profiles. At times wireline density logs are not acquired within the top depth intervals of drilled boreholes, the rock density is extrapolated from the top of a density log to the surface (seafloor for offshore boreholes) to more accurately determine a complete S_v profile. This study uses several extrapolation methods: 1) using wireline sonic logs to convert compressional velocity to density values in boreholes where checkshot data or vertical seismic profile (VSP) surveys are available (Kereru-1, Hawke Bay-1, Opoutama-1, Whakatu-1, Ngapaeruru-1, Tawatawa-1, and Titihaoa-1), 2) using average densities from nearby boreholes with similar stratigraphy (e.g. boreholes Kauhauroa-1, Kauhauroa-2, Kauhauroa-5, Makareao-1, and Tuhara-1A are all within <20 km of each other), or 3) using standard Gardner's relationship (Gardner et al., 1974) and/or regional Gardner's relationship (Table S5 in in Supporting Information S1) to convert compressional velocity data from sonic wireline logs to density data logs (e.g. Hawke Bay-1, Rere-1). All density logs used in this study, supplied by the New Zealand Petroleum and Minerals group (NZPM), have been undergone borehole environmental corrections.

3.3 Minimum principal stress magnitude (σ_3)

σ_3 can be measured directly from pressure-time plots produced during leak-off tests (LOTs), extended leak-off tests (XLOTs), or mini-frac tests (Addis et al., 1998; Bell, 2003; White et

al., 2002; Zoback et al., 2003). In the HSM, LOTs are the most common tests available to calculate *in-situ* σ_3 magnitudes. LOTs are pumping pressure tests conducted in a borehole a few meters below recently set casing shoes. During constant fluid volume pumping, the recorded fluid pressure increase stops behaving linearly with time as the injected fluid pressure surpasses the σ_3 confining stress around the borehole and fluid starts to penetrate into the formation around the borehole (Addis et al., 1998; Bell, 1996). The point when the fluid pressure-time curve becomes non-linear (leak-off pressure (LOP)) can be read as an approximation of σ_3 magnitude. If a LOT is stopped at any point before the LOP is reached the test is called a formation integrity test (FIT) and fluid pressure has not exceeded σ_3 magnitude. In this case, the final fluid pressure value recorded during the FIT can be used as an estimate of the lower boundary of the σ_3 magnitude (e.g. Makareao-1, Zoback et al., 2003).

In the majority of boreholes studied here the validity and accuracy of LOTs cannot be assessed as the pressure–time record data is not fully reported, with only the final LOP being provided in the text reports by drilling companies. Furthermore, pressure–time records are sometimes estimated by only a few distinct data points, obtained from pressure measurements on fluctuating gauges or flow rate estimations from counting pump strokes, making it impossible to determine the specific and accurate LOP values (Zoback, 2007). It is therefore possible for σ_3 to be reported slightly higher or extremely close to S_v when the measurements are not carefully taken or reported. Further consideration for subduction margins is provided by Couzens-Schultz and Chan (2010), who demonstrate that in active compressional settings and seismically active regions, LOTs cause shear failure along pre-existing fractures rather than generating new tensile fractures, leading to an underestimation of the σ_3 magnitude.

We first calculate σ_3:S_v for all boreholes for which LOP measurements are available and then use the average of these data to extrapolate the σ_3 values beyond the depth of measurements. The FIT:Sv and σ_3:S_v =1 are used to define the lower and upper limit of the σ_3 profile, respectively.

3.4 Maximum horizontal stress magnitude (S_{Hmax})

3.3.1 S_{Hmax} estimation from borehole failure analysis

When a vertical borehole is drilled into a homogeneous, isotropic, and elastic medium parallel to one of the three principal stress orientations, the stress at the borehole wall is

redistributed regarding to non-uniform, far-field principal stresses (Jaeger et al., 2009; Zoback, 2007). Assuming far field principal stresses are vertical and horizontal, the local principal effective stresses at a vertical borehole wall can be defined (Moos & Zoback, 1990; Zoback, 2007):

$$\sigma_{\theta\theta}=S_{Hmax}+S_{hmin}-2\cos 2\theta\ (S_{Hmax}-S_{hmin})-Pp-APRS \quad (2a)$$

$$\sigma_{ZZ}=S_v-2\vartheta\cos 2\theta\ (S_{Hmax}-S_{hmin})-Pp \quad (2b)$$

$$\sigma_{rr}=APRS-P_p \quad (2c)$$

where $\sigma_{\theta\theta}$ is the effective hoop stress (acting parallel to the borehole wall), σ_{ZZ} is the effective vertical stress, σ_{rr} is the effective radial stress (acting perpendicular to the borehole wall), S_{Hmax} and S_{hmin} are the maximum and minimum horizontal principal stress magnitudes, ϑ is Poisson's ratio, APRS is the annulus pressure at the time of borehole failure (or mud weight pressure), P_p is pore pressure, and θ is the angle between the edge of borehole breakout and the S_{Hmax} orientation (Figure 2a & 2b).

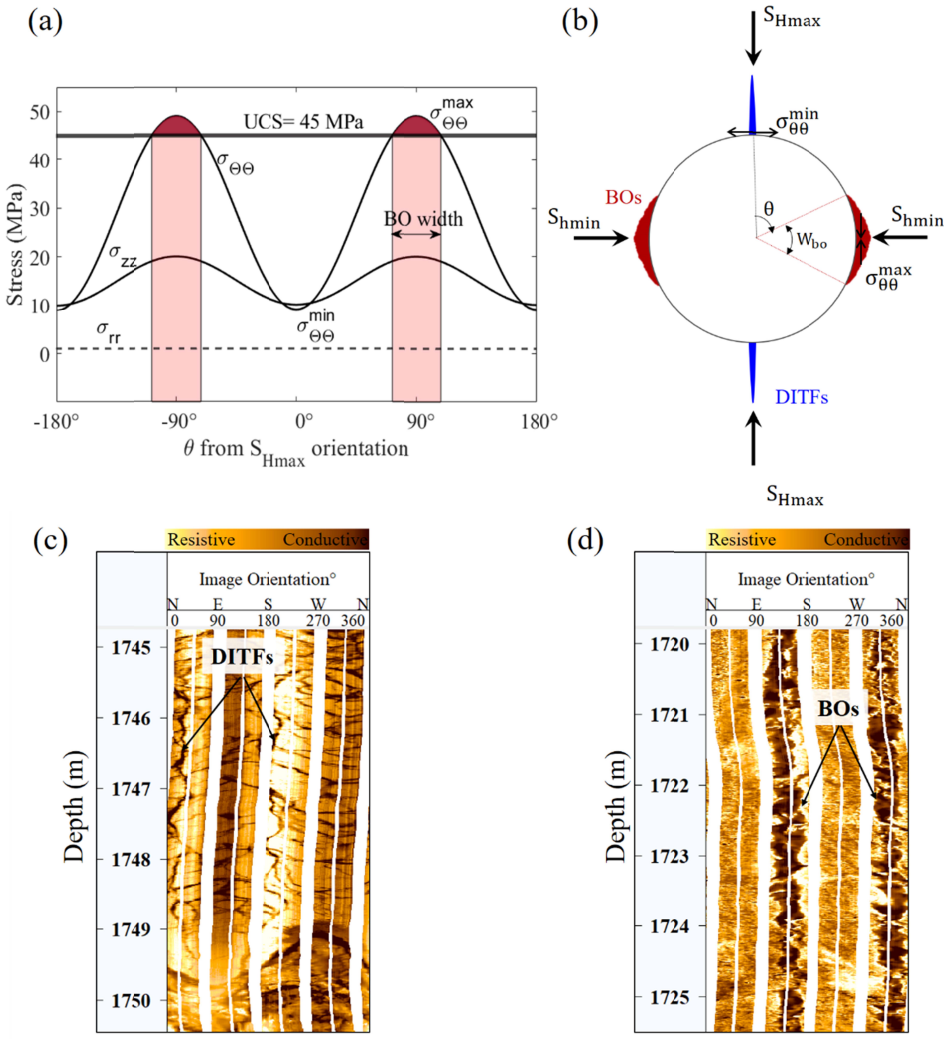

Figure 2. (a) Borehole schematic showing local principal stresses ($\sigma_{\theta\theta}$, σ_{zz}, and σ_{rr}) at the borehole wall as a function of azimuth (θ) measured relative to S_{Hmax} orientation and presence of breakouts for an example in which S_{Hmax} = 50 MPa, S_v = 45 MPa, S_{hmin} = 40 MPa, and UCS=45 MPa. The red shaded region shows schematically the circumference where $\sigma_{\theta\theta}$ is large enough to exceed the compressional strength of the formation and induce BOs. (b) Diagram of a borehole cross-section showing the relationship between BOs, DITFs, and the horizontal principal stress orientations. (c) Example of DITFs as they appear on a resistivity image log. (d) Examples of BOs as they appear on a resistivity image log. Figures 2c-d are from resistivity image logs of borehole Kauhauroa-5. Abbreviations: UCS = unconfined compressive strength; BO = borehole breakout; DITF: drilling induced tensile fracture.

Where local effective stresses exceed the tensile or compressive rock strength of the formation around the borehole, borehole failures such as drilling induced tensile fractures (DITFs) and borehole breakouts (BOs) can form, respectively (Figure 2a). Measurements of the properties of these borehole failures, e.g. the azimuth angle of BOs and/or DITFs and the

angular width of BOs can be used to determine *in-situ* principal stress orientations and to calculate in situ stress magnitudes present at the time of drilling.

DITFs form on the borehole wall where local effective stress concentrations around the borehole wall lead to a minimum $\sigma_{\theta\theta}$ less than the tensile strength of the rock ($\sigma_{\theta\theta}^{\min} \leq 0$) (Aadnoy, 1990), at a borehole azimuth parallel to S_{Hmax} (θ=0°/180°) (Figure 2b) (Aadnoy, 1990; Bell, 2003; Bell & Gough, 1979; Brudy & Zoback, 1999). DITFs typically appear as narrow, conductive (on resistivity image logs) or low amplitude and slower travel time (on acoustic image logs) pairs, ~180° from each other around the borehole wall circumference (Figure 2c). DITFs are generally parallel or slightly inclined to the borehole axis in vertical to semi-vertical boreholes (Brudy & Zoback, 1999; Zoback, 2007). Where DITFs are observed the magnitude of the far-field S_{Hmax} can be constrained using Equation 4 (Zoback, 2007):

$$3S_{hmin} - T_0 - P_p - APRS - \sigma^{\Delta T} \leq S_{Hmax} \quad (3)$$

where S_{Hmax} and S_{hmin} are maximum and minimum horizontal principal stresses respectively, T_0 is the formation tensile strength, P_p is pore pressure, APRS is annulus pressure (or mud weight), and $\sigma^{\Delta T}$ is thermal stress arising from the difference between the drilling mud temperature and formation temperature. $\sigma^{\Delta T}$ is applied where there is a noticeable difference between mud and rock temperature, such as geothermal boreholes. The tensile rock strength in sedimentary rocks is often quite small (a few MPa) and can be assumed to be zero in the analysis of DITFs (Brudy & Zoback, 1999). In this study, $\sigma^{\Delta T}$is considered negligible.

BOs form as enlargements of the borehole diameter on opposite sides of the borehole wall where $\sigma_{\theta\theta}$ is large enough to exceed the formations compressional strength (Figure 2a) (Bell & Gough, 1979; Zoback, 2007). The $\sigma_{\theta\theta}$ magnitude reaches a maximum at θ=±90° (Figure 2a), which occurs at a borehole azimuth oriented perpendicular to the S_{Hmax} direction (Figure 2b). BOs typically appear as a pair of wide, out-of-focus, conductive (in water-based mud; Figure 2d) or resistive (in oil-based mud) zones on resistivity image logs, or as zones of low acoustic amplitude and slower travel time on acoustic image logs. BOs are located ~180° from each other around the circumference of the borehole wall (Figure 2b & 2d). S_{Hmax} magnitudes can be estimated by measuring BO widths (W_{bo}) from borehole image logs using Equation 5 (Barton et al., 1988; Vernik & Zoback, 1992):

$$S_{Hmax} = \frac{(UCS + P_p + APRS + \sigma^{\Delta T}) - S_{hmin}(1 + 2\cos(\pi - W_{bo}))}{1 - 2\cos(\pi - W_{bo})} \quad (4)$$

where W_{bo} is the angular width of the BO; UCS is unconfined compressive strength of the formation, P_p is pore pressure, APRS is annulus pressure or mud weight, S_{hmin} is the minimum horizontal principal stress magnitude, and $\sigma^{\Delta T}$ is the thermal stress effect resulting from the difference between the drilling mud temperature and formation temperature. In this study, $\sigma^{\Delta T}$is considered negligible.

UCS is a key parameter in estimating S_{Hmax} magnitude (Equation 4), and can either be directly measured from laboratory strength tests on core samples, or estimated using empirical relationships between UCS and other rock properties (Chang et al., 2006). Direct measurements of rock strength are rare for the HSM. Borehole Waingaromia-2 in the northern HSM is the only borehole where a laboratory strength test was conducted on calcareous claystone and mudstone core samples (acquired from 132 and 362 m measured depth, respectively), providing UCS values of 1.1-1.2 MPa and friction angles of 20.5°-32.1° (friction coefficient 0.37-0.64) (Indo-Pacific Energy (NZ) Ltd., 2002). However, no relationship between P-wave slowness (Δt_c) and UCS was established because no geophysical logs were obtained and velocity measurements on core samples are unavailable. Therefore, in this study, UCS values are indirectly estimated by using empirical relationships between rock strength and Δt_c. Empirical equations have been developed for different rock types, relating various rock properties to UCS across the world. In this study we utilize a variety of empirical relationships between UCS and sonic velocity by matching appropriate equations to dominant lithologies encountered along each studied borehole in an effort to reduce uncertainty in UCS values and thus S_{Hmax} magnitude values. Upper and lower bounds of the UCS are determined using various published empirical relationships (Chang et al., 2006) to provide a range of possible S_{Hmax} magnitudes (Figure 3). Details on the equations used in individual boreholes to determine the lower and upper limits of UCS can be found in Table S1, Table S2, and S3 in Supporting Information S1.

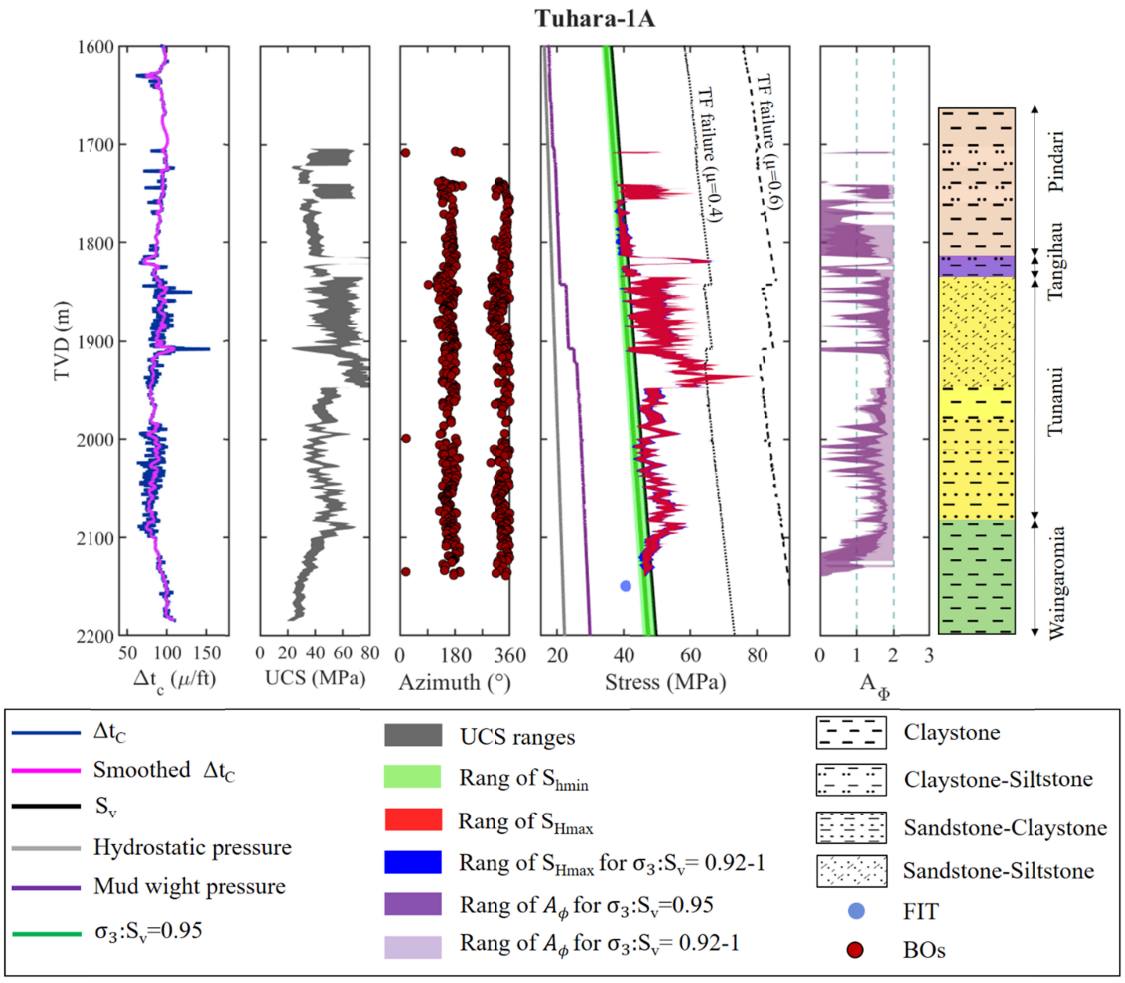

Figure 3. Calculated far-field in situ stress magnitudes, referenced to the sea level in borehole Tuhura-1A. (a) P-wave slowness (blue line) de-spiked and smoothed over 3m intervals (pink line). (b) Range of UCS values derived from P-wave slowness using relations in Table S2 and S3 (c) Azimuth of borehole BOs. (d) Calculated S_v (solid black line), S_{hmin} (green field), and S_{Hmax} (red field) magnitudes by considering that pore pressure is equal to mud weight. The hydrostatic pressure (grey line) is computed assuming a sea water density of 1.03 g/cc. The σ_3 and the range of S_{hmin} is determined from the average σ_3:Sv = 0.95 and σ_3:Sv = 0.92-1, respectively. Abbreviations: Δt_C: P-wave slowness; UCS = uniaxial compressive strength; BO = borehole breakout; FIT = formation integrity test; TF failure: thrust faulting failure; μ: friction coefficient; S_v: vertical stress; S_{hmin}: minimum horizontal stress; S_{Hmax}: maximum horizontal stress; σ_3: minimum principal stress; A_ϕ: Tectonic stress regime index.

A further important parameter required to calculate S_{Hmax} magnitudes and effective stresses is P_p. Direct P_p measurements tests such as RFTs and MDTs are the most reliable measurements (Gunter & Moore, 1986; Zoback, 2007). However, these direct Pp measurements are difficult to acquire, particularly in low permeability formations, and are often only conducted at

depths where possible overpressures may exist (Dutta et al., 2021; Lee et al., 2022; Y. Z. Ma & Holditch, 2015; Zoback, 2007). Drilling mud weight logs can provide indirect, continuous approximations of the Pp along a borehole, and can be used as a proxy of P_p assuming the mud weights have been chosen to stabilize the borehole during drilling, and if no significant mud losses or kicks are reported (Van Ruth et al., 2002) . Mud Losses of greater than 25 bbl/hr for water-based mud (Zhang & Yin, 2017) may indicate that annulus pressure exceeded Pp or/and σ_3 value, resulting in the loss of fluids into the formation. While kicks and high fluid influx indicate that Pp is greater than the annulus pressure. In both cases, the Pp derived from drilling mud weight logs should be corrected to generate a good estimation of Pp. In this study we use mud weight logs from 44 boreholes to calculate Pp. Minor seepage (mud losses <22 bbl/hr) is reported for boreholes Kauhauroa-2/5, Makareao-1, Tuhara-1A, Ngapaeruru-1, Tawatawa-1, and Titihaoa-1, and Ranui-2 in the intervals where BOs are observed, providing confidence in the use of mud weight logs in those intervals for Pp determination. A minor mud loss of 28 bbl/hr has been observed at severely fractured depth interval of 1030-1225 m TVD in borehole Ngapaeruru-1 which was treated by remedial techniques and procedures easily. Moreover, minor background gas and fluid influx are reported in boreholes Kahauuroa-5, Makareao-1, Tuhara-1A, Tawatawa-1, and Titihaoa-1, which were controlled by mud weight such that they never flowed. Since no significant mud losses or kicks are reported in the depth intervals where BOs are observed, we consider the annulus pressure records a good proxy of Pp in those depth intervals.

The P_p calculated from mud weight logs in Kauhauroa-5 and Titihaoa-1 boreholes are further calibrated using direct P_p measurements obtained from RFTs. Formation tests conducted in 17 further HSM boreholes (Awatere-1, Hukarere-1, Kauhauroa-2/3/4B, Kiakia-1A, Makareao-1, Mangaone-1, Morere-1, Opoutama-1, Ruakituri-1, Takapau-1, Te Hoe-1, Tuhara-1A/1B, Waitahora-1, and Waitaria-2) are not included in this study due to incomplete pressure build ups during testing in low-permeability formations, test seal failures, or tests conducted in formation intervals supercharged to hydrostatic pressure.

3.3.2 S_{Hmax} magnitude estimation from frictional limit theory

To constrain S_{Hmax} magnitudes that result in the observed BO and DITF occurrences, the stress state is assumed to be limited by Coulomb frictional sliding on an optimally oriented and pre-existing fault plane (Zoback, 2007). This means that the maximum effective principal

stress cannot exceed the stress value required to cause slip, defined by the friction coefficient (μ) of adjacent faults, on a critically oriented fault plane (Jaeger et al., 2009; Sibson, 1974):

$$\frac{(\sigma_1 - P_p)}{(\sigma_3 - P_p)} \leq ((1 + \mu^2)^{0.5} + \mu)^2 \quad (5)$$

where σ_1 is the maximum principal stress, σ_3 minimum principal stress, P_p is pore pressure, and μ is coefficient of friction on an optimally oriented, cohesionless, pre-existing fault.

This constraint is typically displayed as a stress polygon, which shows the permissible values of horizontal principal stress magnitudes for a specific depth, S_v, μ, and P_p for normal, strike-slip, and thrust faulting tectonics (Zoback, 2007). Although this method only provides the upper and lower limits for the S_{Hmax} magnitude, it can yield more accurate ranges of permissible S_{Hmax} magnitudes when combined with S_{Hmax} magnitude estimates from borehole failure analysis (Chang et al., 2010; Huffman & Saffer, 2016).

3.5 Tectonic stress regime index (A_ϕ)

In order to characterize a stress regime or faulting style with stress magnitude data, we use the stress regime index (A_ϕ, Equation 6a and 6b) described by Simpson (Delvaux et al., 1997):

$$A_\phi = (n + 0.5) + (-1)^n (R - 0.5) \quad (6a)$$

$$R = (\sigma_2 - \sigma_3) / (\sigma_1 - \sigma_3) \quad (6b)$$

where n is the number of principal stress components greater than the principal stress whose axis is closest to the vertical, R is the stress ratio, and σ_1 , σ_2 , σ_3 are the maximum, medium, and minimum principal stress magnitudes, respectively.

A_ϕ values range from 0 to 1 in normal faulting regimes, 1 to 2 in strike-slip regimes, and 2 to 3 in thrust faulting regimes.

4 Results

4.1 Vertical Stress Magnitudes

S_v magnitudes determined from 24 onshore boreholes provide overburden stress gradients ranging from 20.92 to 26.97 MPa/km, with a mean value of 22.58± 1.23 MPa/km (Figure 4a; Table S5). S_v magnitudes measured within the 3 offshore boreholes range from 20.9 to 21.7 MPa/km with a mean value of 21.26± 0.4 MPa/km.

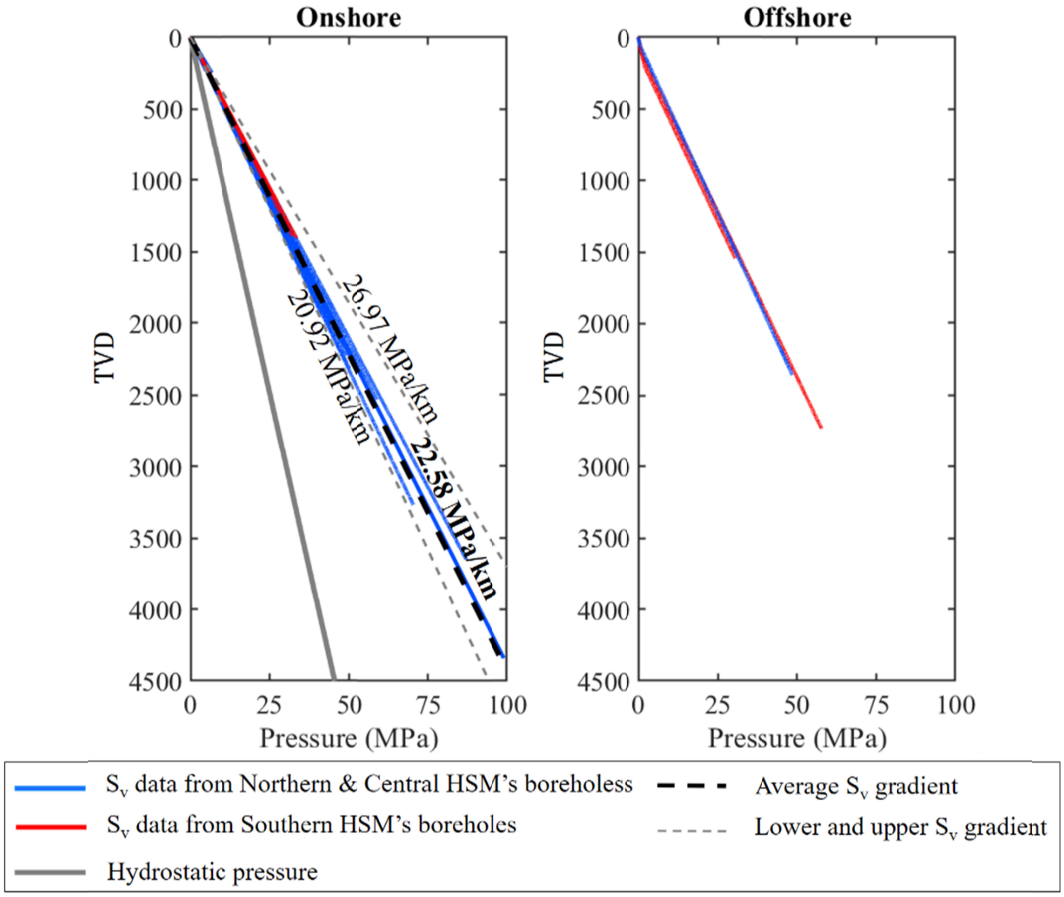

Figure 4. S_v gradient profiles from boreholes in the a) HSM onshore and b) HSM offshore. S_v: vertical stress.

4.2 Minimum Principal Stress Magnitudes

σ_3 magnitudes calculated from LOT data range from 1.9 MPa at 102.3 m TVD (borehole Waitaria-2) to 77.9 MPa at 3610.6 m TVD (borehole Rere-1) (Table 1). For all examined LOT data (with the exception of one test in borehole Titihoa-1 where σ_3 derived from LOP is greater than S_v), the normalized effective σ_3 ratio ranges from 0.23 to 1 (Table 1).

Table 1. σ_3 magnitudes calculated from LOP measurements.

	Borehole	Depth[a] (m)	σ_3[b] (MPa)	S_v[c] (MPa)	σ_3/S_v
Central HSM	Awatere-1	301.9 1085.3	6.1 22.4	6.5 24.0	0.94 0.93
	Hawke Bay-1	386.6 1359.6	7.2 26.4	7.4 27.7	0.97 0.95
	Kauhauroa-1	455.8	7.9	9.5	0.83
	Kauhauroa-2	463.8	8.2	10.1	0.81
	Kauhauroa-5	459.2	7.4	10.2	0.73
	Kereru-1	481.1	9.4	10.2	0.92
	Kiakia-1/1A	318.6	5.7	6.9	0.83

	Opoho-1	521.3	9.3	11.7	0.79
	Rere-1	3610.6	77.9	82.3	0.95
	Tuhara-1/1A	590.8	8.4	13.3	0.63
	Waitaria-2	102.3	1.9	2.4	0.79
Southern HSM	Ranui-1	357.3	5.2	8.6	0.6
	Tawatawa-1	722.5	12.7	12.7	1
	Titihaoa-1	614.9	9.5	11	0.86
		1585.7	30.6	32.4	0.94
		1979.8	43.4*	41.3	1.05

[a] True vertical depth from ground level for onshore boreholes and sea level for offshore boreholes

[b] σ_3 derived from Leak-off pressure

[c] S_v vertical stress

* σ_3 derived from LOP is greater than S_v

LOP values measured in boreholes Tuhara-1/1A and Ranui-1 (11 m west of Ranui-2) are remarkably low, such that LOP values are less than the σ_3 values estimated by normal faulting failure with friction coefficients less than 0.6. In borehole Titihoa-1, the σ_3 value (43.4 MPa) derived from an LOT performed at ~1979.8 m TVD is greater than the S_V for this depth (41.3 MPa). In this case, σ_3 is considered to be vertical, indicating a thrust/reverse faulting regime (Zoback, 2007). In borehole Tawatawa-1 two LOTs were performed at 722.5 m TVD. The initial test yielded a LOP of 13.23 MPa, while the second LOT yielded a LOP of 13.36 MPa (Tap Oil Limited, 2004). Our reassessment of pressure-time curve of the second LOT (which had more data defining the time-pressure plot) reveals that the formation breakdown pressure (FBP) was reported rather than LOP, resulting in an overestimation of σ_3 making it appear greater than the S_v for this depth. We determine the LOP of the second test by intersecting the straight line of the linear section with the tangent line of the ascending section on the pressure-volume curve (Figure 5), and report a σ_3 magnitude of 12.7 MPa, almost equal to S_v (13 MPa). Assuming σ_3 measurements made from the reported LOT data in the study boreholes are a proxy of σ_3 (after correcting σ_3 derived from LOP $>S_v$ to $\sigma_3=S_v$), a HSM average minimum normalized effective stress ratio of 0.66±0.2 and 0.7±0.3 are derived for the central and southern HSM respectively (Figure 6).

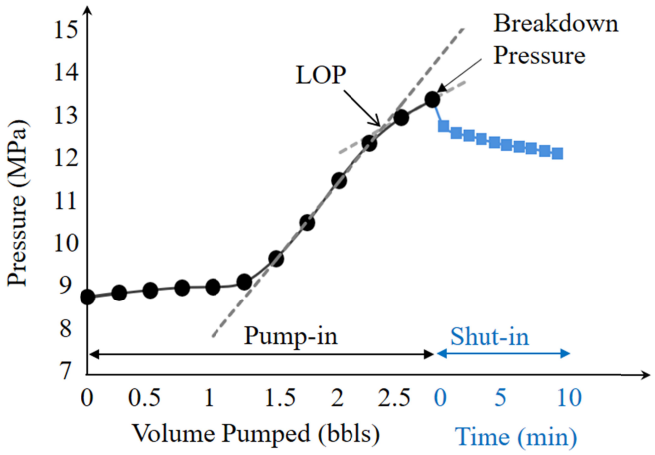

436

437 **Figure 5.** Results of the leak-off test run at 722.5 m TVD in borehole Tawatawa-1. Pressure versus
438 volume of mud pumped to the formation curve reveals that the leak-off pressure (LOP) is 12.7 MPa.

439 FIT data show the lower limit of σ_3 magnitudes are typically below S_v in most of boreholes in
440 this study. However, in some boreholes (Table 2), FIT results are approximately equal to or
441 greater than S_V. The entire FIT dataset for all boreholes in this region can be found in Table
442 S3 in Supporting Information S1, and are used to constrain σ_3 profiles within boreholes where
443 LOP measurements are not available.

444

445 Table 2. The lower limit of σ_3 values calculated from FIT data.

	Borehole	Depth[a] (m)	The lower limit of σ_3[b] from FIT[c] (MPa)	S_v[d] (MPa)
Central HSM	**Hukarere-1**	89.9 430.2	1.81 8.64	1.69 8.55
	Kauhauroa-3	332.7 999.2	7.33 22.44	7.42 22.56
	Kauhauroa-4	346.1	7.63	7.36
	Kauhauroa-4B	91 538.3	1.95 11.56	1.97 11.75
	Makareao-1	306.2 484.8	6.76 10.6	6.55 10.59
	Rere-1	115 2109.4	2.39 49.56	2.65 48.17
	Waitahora-1	95.8 722 994.5	2 16.24 22.93	2.01 15.53 21.76
	Waitaria-2	556.1	12.53	12.85

446 [a] True vertical depth from ground level for onshore boreholes and sea level for offshore
447 boreholes
448 [b] Minimum principal stress magnitudes
449 [c] Formation integrity test
450 [d] S_v vertical stress
451

We calculated σ_3:S_v (after correcting σ_3 derived from LOP and FIT >S_v to σ_3=S_v) for all 21 LOTs and 39 FIT measurements in the study area and found that σ_3:S_v varies significantly above and below 650-700 m TVD (Figure 6). The σ_3:S_v ranges from 0.6-1 at depths above 650-700 m TVD, while it ranges from 0.92-1 below this depth interval (Figure 6). Above and below 650-700 m TVD, the average σ_3:Sv values derived from LOT measurements are 0.79 and 0.95, respectively.

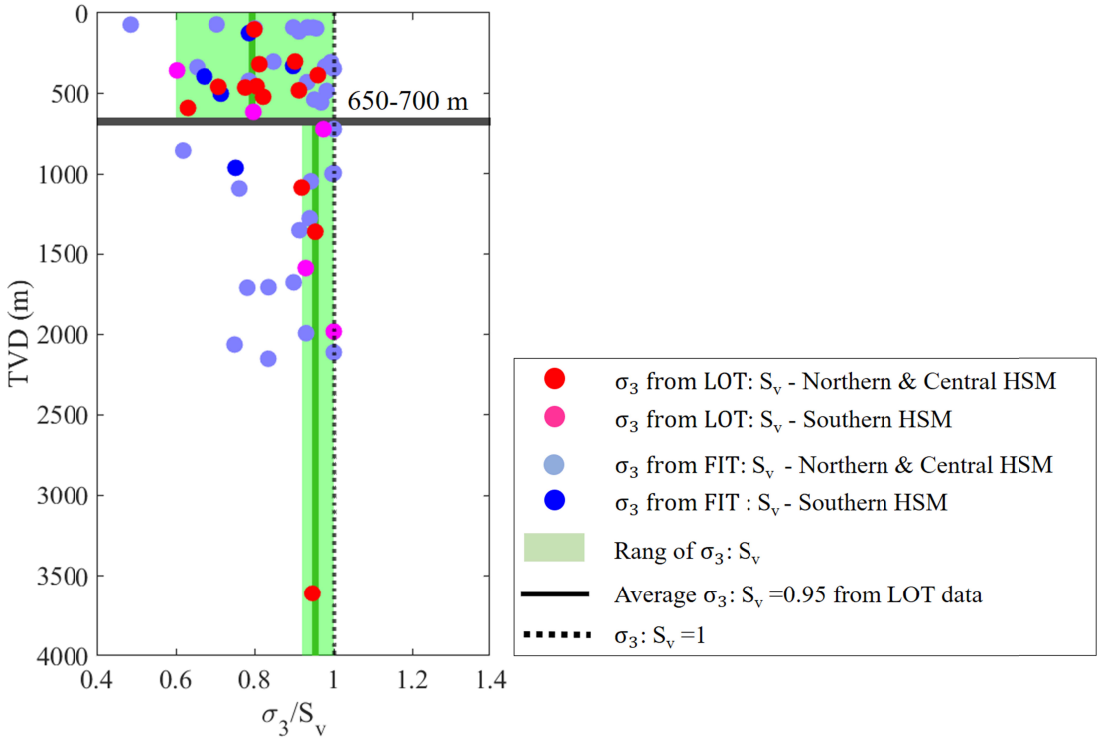

Figure 6. σ_3: S_v along the HSM. Abbreviations: LOT: leak of test; FIT = formation integrity test; S_v: vertical stress; σ_3: minimum principal stress.

In this study, to create the σ_3 profile in boreholes where LOT measurements are not available at the depth of interest, we only consider LOT and FIT measurements recorded at depths below 650-700 m TVD for two main reasons: 1) to exclude the influence of topographic effects and shallow processes such as gravitational collapse, erosion, and subsidence in the σ_3 calculation, and 2) because our borehole breakouts data to estimate S_{Hmax} magnitudes in 7 out of 8 boreholes are located below 700m TVD.

4.3 Stress magnitude from borehole data

4.3.1 Central HSM (Hawke's Bay region)

A range of potential S_{Hmax} magnitudes are estimated along individual boreholes at depths intervals where BO widths and DITFs are measured from image logs. Further the lower and

upper limit of S_{Hmax} magnitudes are constrained by theoretical limits provided by slip on pre-existing faults with a friction coefficient of 0.6 (described in 3.3.2).

Makareao-1 borehole

The σ_3 :S_v ratios of 1.03 and 1 are determined from σ_3 values calculated using FIT data at depths 306.2 and 484.8 m TVD respectively (Table 2). The σ_3 :$S_v \geq 1$ indicates that $\sigma_3 = S_v$ in this borehole. The S_{Hmax}:S_v ratio of 1.03-1.31 is determined for borehole Makareao-1 using the S_{Hmax} values calculated from the lower and upper value of UCS.

The S_{Hmax}:S_v ratio of 1.03-1.31 and a σ_3 :S_v =1 along this borehole indicates a stress regime such that $\sigma_3 = S_v < S_{Hmax}$ (Figure 7a). A_ϕ =2 is determined from calculated stress magnitude data in this borehole.

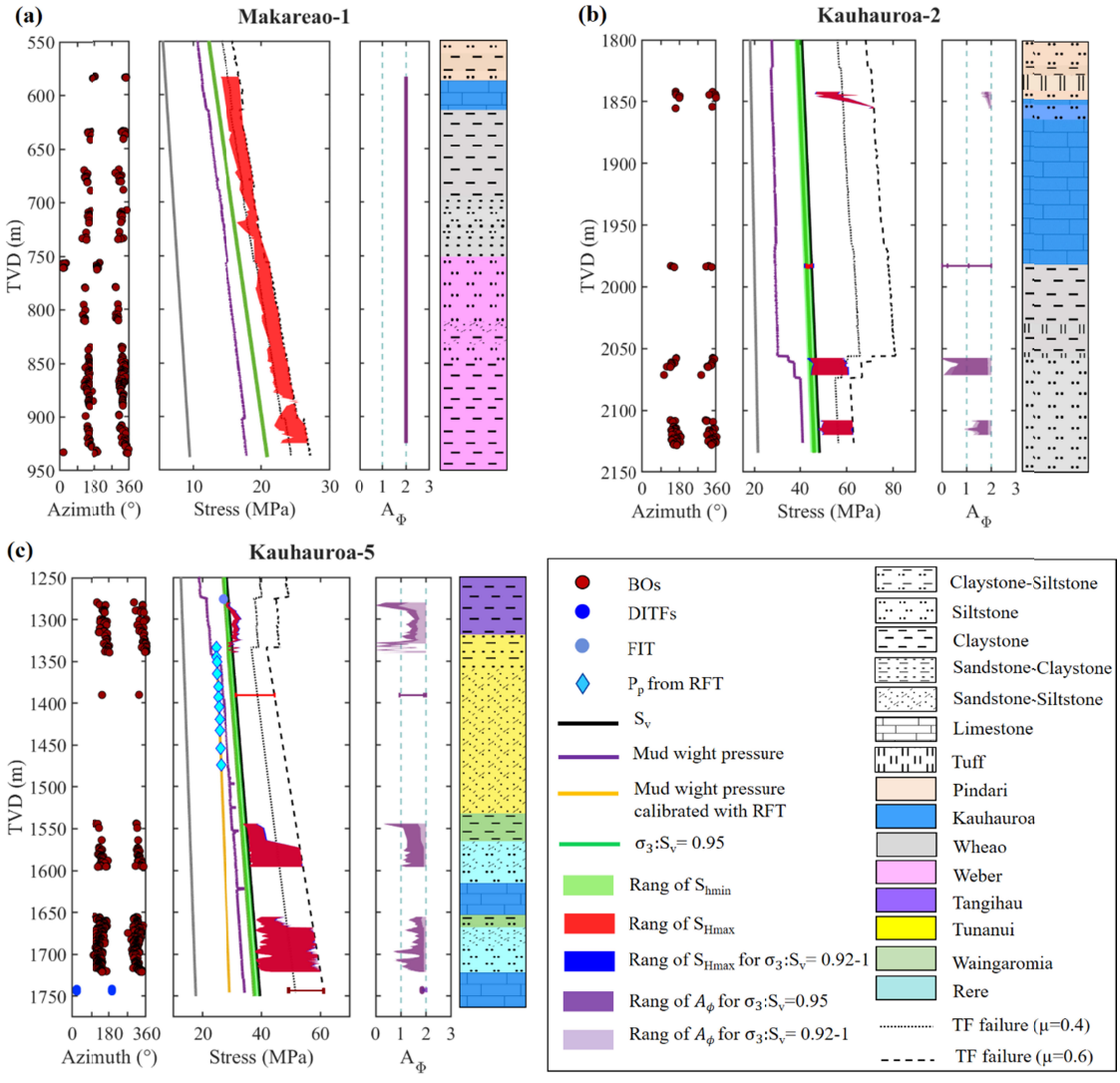

Figure 7. Calculated far-field in situ stress magnitudes, referenced to the sea level in borehole (a) Makareao-1 (b) Kauhauroa-2 (c) Kauhauroa-5 in the central HSM. Abbreviations: Δt_C: P-wave slowness; UCS = uniaxial compressive strength; BO = breakout; DITF: drilling induced fracture; FIT = formation integrity test; TF failure: thrust faulting failure; μ: friction coefficient; RFT: repeat formation test; S_v: vertical stress; S_{hmin}: minimum horizontal stress; S_{Hmax}: maximum horizontal stress; σ_3: minimum principal stress; A_ϕ: tectonic stress regime index.

Kauhauroa-2 borehole

A σ_3 :S_v ratio of 0.81 is determined from σ_3 value calculated using LOT data at 463.8 m TVD (Table 1). The σ_3 values in the deeper part of the borehole are calculated from the average σ_3 :S_v ratio of 0.95 along the HSM and are further constrained by the lower limit of σ_3 value determined from an FIT= 30.23 MPa at 1707.3 m TVD. The S_{Hmax}:S_v ratio of 0.95-1.71 is determined for borehole Kauhauroa-2 using the S_{Hmax} values calculated from the lower and upper value of UCS.

The S_{Hmax}:S_v ratio of 0.95-1.71 and the σ_3 :S_v ratio of 0.95 indicate a dominant stress regime such that $S_{hmin} \leq S_v \leq S_{Hmax}$ (Figure 7b). A $0 \leq A_\phi \leq 1.94$ is determined from calculated stress magnitude data in this borehole. S_v, S_{hmin}, and the lower limit of S_{Hmax} are nearly equal below 1980 m TVD such that $S_{hmin} \approx S_{Hmax} \approx S_v$.

Kauhauroa-5 borehole

A σ_3 :S_v ratio of 0.73 is determined from σ_3 value calculated using LOT data at 459.2 m TVD (Table 1). The σ_3 values in the deeper part of the borehole are calculated from the average σ_3 :S_v ratio of 0.95 along the HSM and are further constrained by the lower limit of σ_3 value calculated from an FIT value of 27.13 MPa at 1276.1 m TVD. The S_{Hmax}:S_v ratios of 0.95-1.13 in 1280-1350 m TVD and 0.97-1.54 in 1390-1750 m TVD are determined in this borehole using the S_{Hmax} values calculated from the lower and upper value of UCS.

The analysis of S_{Hmax} magnitudes and the σ_3 :S_v ratio of 0.95 indicate a dominant $S_{hmin} \approx S_v \approx S_{Hmax}$ (S_{Hmax}- S_{hmin}<5 MPa) and $0 \leq A_\phi \leq 1.13$ in the depth interval of 1280-1350 m TVD (Figure 7c). Moving along the depth to 1390-1750 m TVD, $S_{hmin} \leq S_v \leq S_{Hmax}$ and $0.44 \leq A_\phi \leq 1.92$ are observed.

Further constraints on stress magnitudes are made in this borehole using the presence of DITFs between 1741-1745 m on FMI borehole image logs (Figure 7c). The presence of DITFs at 1742.3 m suggests that the S_{Hmax} should be above the DITF line (Figure 8), where the local hoop stress can be tensile (Equation 3), but also inside the stress polygon with μ=

0.6. The possible range of S_{Hmax} and S_{hmin} constrained using this information lie inside the blue shaded area (Figure 8) and suggest a stress state such that $S_{hmin} \leq S_v < S_{Hmax}$.

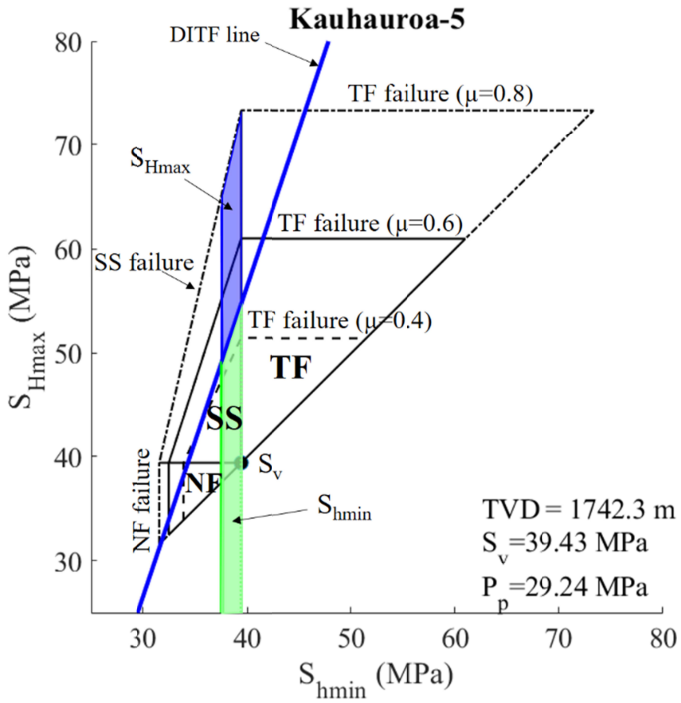

Figure 8. Analysis of stress magnitudes using stress polygon defined by Coulomb friction law with a friction coefficient (μ) of 0.4 and 0.6, and 0.8 in borehole Kauhauroa-5 at depth of 1742.3 m where DITFs are observed. The green shaded area represents σ_3 range estimated from the average σ_3 :S_v ratio of 0.95 along the HSM. The blue shaded area represents S_{Hmax} range which local hoop stress is tensile and DITFs are formed. NF: normal faulting, SS: strike-slip faulting, TF: thrust faulting; DITF: drilling induced tensile fracture.

Tuhara-1A borehole

A σ_3 :S_v ratio of 0.63 is determined from σ_3 value calculated using LOT data at 590.8 m TVD (Table 1). The σ_3 values in the deeper part of the borehole are calculated from the average σ_3 :S_v ratio of 0.95 along the HSM, and are further constrained by the lower limit of σ_3 value determined from FIT value of 40.6 MPa at 2149.5 m TVD. The S_{Hmax}:S_v ratio of 0.95-1.81 is determined for borehole Tuhara-1A using the S_{Hmax} values calculated from the lower and upper value of UCS.

The The S_{Hmax}:S_v ratio of 0.95-1.81 and the σ_3 :S_v ratio of 0.95 indicate a dominant stress regime such that $S_{hmin} \leq S_v \leq S_{Hmax}$ (Figure 3). A $0 \leq A_\phi \leq 1.95$ is determined from calculated stress magnitude data in this borehole.

4.2.2 Southern HSM

Ngapaeruru-1 borehole

The σ_3 values in this borehole are calculated from the average σ_3 :S_v ratio of 0.95 along the HSM and are further constrained by the lower limit of σ_3 value determined from FIT values of 8.35 and 16.86 MPa at 501.9 and 962.7 m TVD, respectively. The S_{Hmax}:S_v ratio of 0.95-1.75 is determined for borehole Ngapaeruru-1 using the S_{Hmax} values calculated from the lower and upper value of UCS.

The S_{Hmax}:S_v ratio of 0.95-1.75 and the σ_3 :S_v ratio of 0.95 indicate a dominant stress regime such that $S_{hmin} \leq S_v \leq S_{Hmax}$ (Figure 9a). A $0 \leq A_\phi \leq 1.94$ is determined from calculated stress magnitude data in this borehole (Figure 9a). The upper limit of S_{Hmax} magnitudes from the upper values of UCS are constrained by the limits provided by slip on pre-existing faults with μ=0.6.

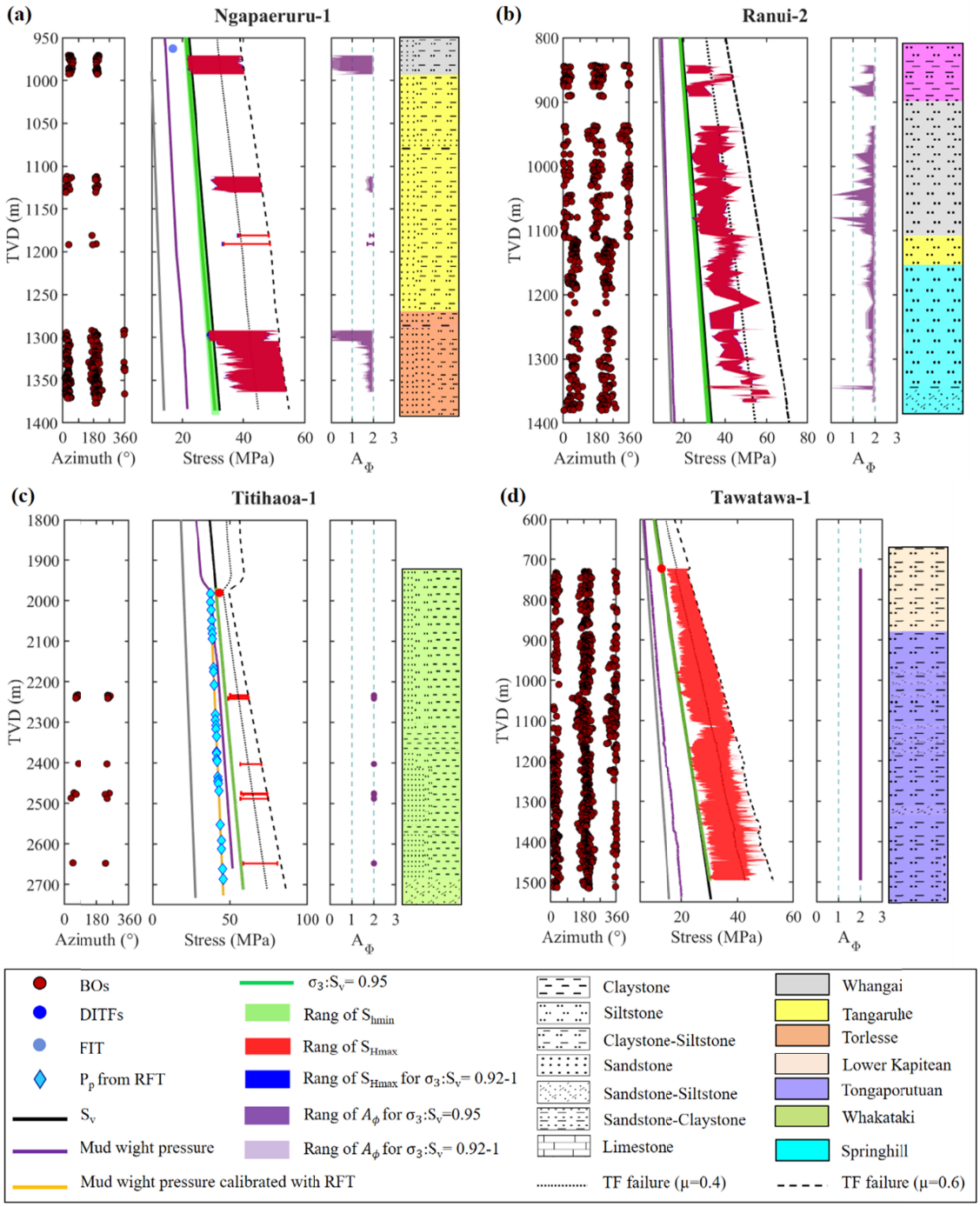

Figure 9. The constrained in situ stress profile with depth in (a) Ngapaeruru-1 (b) Tawatawa-1 (c) Titihaoa-1 in the southern HSM. Abbreviations: BO = breakout; FIT = formation integrity test; LOT: leak of test; TF failure: thrust faulting failure; μ: friction coefficient; RFT: repeat formation test; S_v: vertical stress; S_{hmin}: minimum horizontal stress; S_{Hmax}: maximum horizontal stress; σ_3: minimum principal stress; A_ϕ: tectonic stress regime index.

553 **Tawatawa-1 borehole**

554 A σ_3 :S_v ratio of 1 is determined from σ_3 value calculated using LOT data at 722.5 m TVD
555 (Table 1). The S_{Hmax}:S_v ratio of 1-1.82 is determined for borehole Tawatawa-1 using the
556 S_{Hmax} values calculated from the lower and upper value of UCS.

557 The S_{Hmax}:S_v ratio of 1-1.82 and the σ_3 :S_v =1 indicate a dominant stress regime such that σ_3 =
558 $S_v \leq S_{Hmax}$ (Figure 9d). The upper limit of S_{Hmax} magnitudes from the upper values of UCS
559 are constrained by the limits provided by slip on pre-existing faults with μ=0.6. A_ϕ =2 is
560 determined from calculated stress magnitude data in this borehole.

561 **Titihaoa-1 borehole**

562 The σ_3 :S_v ratios of 0.86, 0.94, and 1.05 are determined from σ_3 values calculated using LOT
563 data at 614, 1585.7, and 1979.8 m TVD in this borehole (Table 1). The σ_3 :S_v ratio of 1.05 at
564 1979.8 m TVD indicate that $\sigma_3 = S_v$ at depth intervals of 2200-2700 m TVD. The S_{Hmax}:S_v
565 ratio of 1.02-1.41 are determined for borehole Titihaoa-1 using the S_{Hmax} values calculated
566 from the lower and upper value of UCS.

567 The analysis of S_{Hmax} magnitudes and σ_3 :S_v=1 at depth intervals of 2200-2700 m TVD
568 indicate a stress regime such that $\sigma_3 = S_v \leq S_{Hmax}$ (Figure 9c). The upper limit of S_{Hmax}
569 magnitudes from the upper values of UCS are constrained by the limits provided by slip on
570 pre-existing faults with μ=0.6. A_ϕ = 2 is determined from calculated stress magnitude data in
571 this borehole.

572 **Ranui-2 borehole**

573 The σ_3 profile in this borehole is calculated from the average HSM σ_3 :S_v ratio of 0.95 are
574 further constrained by the lower limit of σ_3 value determined from FIT value of 6.35 MPa at
575 395 m TVD. The S_{Hmax}:S_v ratio of 0.95-3.12 are determined for borehole Ranui-2 using the
576 S_{Hmax} values calculated from the lower and upper value of UCS.

577 The The S_{Hmax}:S_v ratio of 0.95-3.12 and the σ_3 :S_v ratio of 0.95 indicate a dominant stress
578 regime such that $S_{hmin} \leq S_v \leq S_{Hmax}$ (Figure 9b). A $0 \leq A_\phi \leq 1.96$ is determined from
579 calculated stress magnitude data in this borehole.

580

581 # 5 Discussion

582 ## 5.1 Shallow HSM tectonics

583 Stress magnitudes calculated from borehole data indicate that the S_{Hmax}:S_v ratios ranging
584 from 0.95-1.81 in the central HSM and 0.95-3.12 in the the southern HSM. Additionally,

585 σ_3:S_v ratios of 0.6-1 are measured at depths above 650-700 m TVD, while 0.92-1 are
586 measured below this depth interval along the HSM. These stress magnitude results reveal that
587 across the central and southern HSM, S_{Hmax} is dominantly σ_1, indicating a thrust to strike-slip
588 faulting regime. The observed dominant thrust to strike-slip faulting regime is consistent with
589 observed contractional tectonics in the HSM developed by the subduction of the Hikurangi
590 Plateau beneath the North Island (Barnes et al., 1998; Nicol & Beavan, 2003), and the strike-
591 slip faulting generated by forearc rotation of the East Coast (Beanland & Haines, 1998;
592 Litchfield et al., 2014; Nicol et al., 2007; Wallace et al., 2004).

593 Behboudi et al. (2022) report a dominant ENE-WSW shallow crust S_{Hmax} orientation within
594 the central HSM, and WNW-ESE or NW-SE S_{Hmax} orientations for the southern HSM
595 (Figure 1b). Considering σ_1=S_{Hmax} along the HSM, observed S_{Hmax} orientations suggest the
596 contemporary maximum compressional stress switches from subparallel (ENE-WSW) to the
597 Hikurangi margin in the north and central HSM, to roughly perpendicular (WNW-ESE or
598 NW-SE) to the Hikurangi margin in the southern HSM. Based on our confirmation here that
599 σ_1=S_{Hmax} along the HSM, it is likely that contemporary tectonics in the central HSM are
600 dominantly strike-slip, while in the southern HSM, more contractional tectonics may be
601 expected.

602 The NNE/NE striking faults in the central HSM, while currently inactive, express reverse
603 dip-slip components to them based on seismic survey data (Western Energy New Zealand,
604 2001). This tectonic slip is at odds with the contemporary fault strike-parallel σ_1 (S_{Hmax}). We
605 suggest here that these central HSM faults formed in an initially contractional stress state
606 such that σ_3= S_v, σ_1=S_{Hmax} oriented NW-SE which would have been consistent with the NW-
607 SE component of Pacific-Australian plate motion. Overtime, this stress state changed from
608 this contractional state to the modern strike-slip/contractional/contractional-oblique stress
609 state (σ_3:S_v=0.92-1, σ_1=S_{Hmax} oriented ENE-WSW).

610 This switch in σ_1 orientation overtime and along HSM strike may be explained by (a) long-
611 term clockwise rotation of the Hikurangi forearc (b) clockwise rotation of the Hikurangi
612 forearc in conjunction with high shallow crust overpressures and/or mechanical property
613 variations, and/or (c) along-strike variation in slip behavior in the HSM.

614 Clockwise rotation of the forearc, which accommodates the margin-parallel component of
615 oblique Pacific-Australian plate motion, drives strike-slip and/or normal faulting within the
616 onshore portion of the northern and central HSM, and transpressional faulting in the southern

HSM (Figure 5, Fagereng & Ellis, 2009; Nicol et al., 2007; Wallace et al., 2004; Wallace, Fagereng, & Ellis, 2012). Behboudi et al. (2022) suggest that this forearc rotation is likely responsible for generating strike-slip stress state with ENE-WSW $S_{Hmax} = \sigma_1$ in the central HSM, and contemporary contractional stress state with WNW-ESE/ NW-SE $S_{Hmax} = \sigma_1$ in the southern HSM. However, our stress magnitude results of $\sigma_3 : S_v = 0.92\text{-}1$ and $\sigma_1 = S_{Hmax}$ leave a possibility for both strike-slip and contractional stress states to occur across both the central and southern HSM due to poorly constrained UCS values used in this study, a limitation of the study that could be restricted by laboratory rock strength testing of both onshore and offshore HSM lithologies.

The northern and central HSM have high Pp based on borehole data (Burgreen-Chan et al., 2016; D. Darby & Funnell, 2001), magnetotellurics (Heise et al., 2019), and seismic tomography (Bassett et al., 2014; Eberhart-Phillips et al., 2017). Overpressure reduces the effective normal stress on fault planes, meaning that the existing NNE/NE striking faults in this region will be able to slip at lower shear stresses. Therefore, as the result of this overpressure, these faults could be less stable, allowing the hangingwall of upper plate faults to move more easily in response to NE-SW forces raised from forearc rotation. In this scenario, forces raised from forearc rotation were able to alter stress state overtime from $\sigma_3 : S_v = 1$ and $\sigma_1 = S_{Hmax}$ with NW-SE S_{Hmax} orientation, compatible with NW-SE component of Pacific-Australian plate motion and old geological structures, to $\sigma_3 : S_v = 0.92\text{-}1$ and $\sigma_1 = S_{Hmax}$ with ENE-WSW S_{Hmax} orientation. Similar shallow, high overpressures are not observed in the hangingwalls of upper plate faults in the onshore of the southern HSM. Therefore it is possible that the NE-SW forces resulted from forearc rotation alone are insufficient to exceed the fault shear resistance and change the orientation of σ_1 away from the NW-SE component of Pacific-Australian plate motion, however they may have been high enough to play a role in reducing σ_3 magnitudes to the point that they become $<= S_v$, resulting in a more transtensional tectonic regime overtime.

The mechanical properties of fault gauges and formations hosting faults (friction coefficient and rock strength) can play a role in controlling upper plate tectonic stresses (Mantovani et al., 2000; Marotta et al., 2002). Reiter (2021) investigated the impact of physical and elastic parameter contrasts on S_{Hmax} orientation and proposed that contrasts in Young's modulus can introduce S_{Hmax} rotations up to 78°, with larger stress rotations occurring within the softer lithologies. Behboudi et al. (2022) proposed that basement uplift in the southern HSM may introduce lateral geomechanical heterogeneities and variations in rock and sediment physical

properties along the HSM which may influence S_{Hmax} orientations. Such that clay and sand-siltstone sediments (Miocene to present), where our stress data are calculated, in the upper plate of the central HSM may geomechanically differ from clay and sand-siltstone sediments (Miocene to Cretaceous) in the onshore of the southern HSM. Therefore, we analyzed physical properties of aforementioned sediments and discovered that P-wave velocity (V_p), UCS ranges, and Young's modulus in the central HSM are lower than the onshore of southern HSM (Figure 10). In this scenario, S_{Hmax} orientations in the sediments of the central HSM, which have lower UCS and Young's modulus, could be easily reoriented in response to long-term forces such as forearc rotation compared to southern HSM. This theory, however, does not explain why the offshore boreholes in the southern HSM have not reoriented in response to long-tern forearc rotation forces, while having comparable V_p, UCS range, and Young's Modulus to the boreholes in the central HSM.

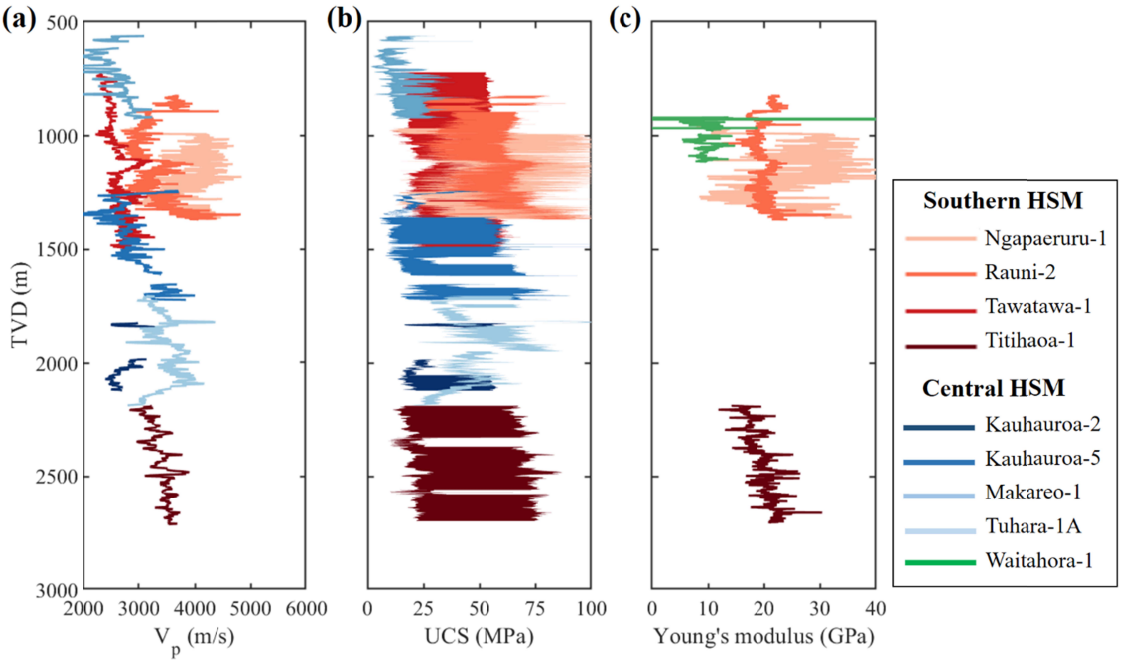

Figure 10. Graph shows (a) p-wave velocity, (b) rock strength (UCS), and (c) Young's modulus in clay and sand-siltstone sediments as a function of depth across the central and southern HSM.

This along-strike variation in contemporary stress state is spatially consistent with north to south variation in slip behavior along the Hikurangi subduction interface (**Figure 1**a). In the northern and central HSM, the subduction interface is largely creeping and experiences shallow (<15 km), episodic slow slip events that extend offshore and possibly to the trench. At the southern HSM the plate interface is strongly interseismically locked to ~30 km depth, and is currently accumulating elastic strain in the surrounding crust (Wallace, 2020). Some

672 studies suggest that SSEs can release the amount of energy equivalent to a M_w 6.5–8
673 earthquakes (Dixon et al., 2014; Wallace, Beavan, et al., 2012). In the central HSM the
674 recurring SSEs and frequent earthquakes may release energy overtime such that the normal to
675 shear stress ratio on pre-existing faults has changed in a way that make it easier to slip in
676 response to forces deriving from long-term forearc rotation. While stress accumulation due to
677 locked nature of the southern HSM, don't allow the normal to shear stress ratio change
678 considerably on the existing NNE/NE striking compressional faults and make it difficult for
679 the hanging wall of these faults to slip in response to forearc rotation forces; therefore stress
680 state has not changed overtime in the southern HSM. However, the static stress drop of SSEs
681 is estimated to range 0.01–1.0 MPa (Gao et al., 2012). Given that the contemporary σ_3:
682 $S_v \approx 0.95$ and S_v-σ_3 ranges between 0-3 MPa (for depths less than 3 km), these SSEs should
683 have existed in the central HSM for more than 20 years such that they were able to release
684 energy in order of 3 MPa (for depths less than 3 km) to change the initial $\sigma_3 : S_v = 1$ to the
685 contemporary $\sigma_3 : S_v = 0.92\text{-}1$ and reorient the S_{Hmax} orientation from NW-SE to ENE-WSW
686 in this region. However, further research and modeling are required to determine and quantify
687 the initial stress state and whether the amount of stress released during SSEs in the central
688 HSM was sufficient to support such a theory.

689 ## 5.2 Extensional tectonics within the HSM forearc

690 There are locales in the central and southern HSM where stress magnitude determination
691 suggests a normal faulting regime (σ_3:$S_v < 1$ and $0 \leq A_\phi \leq 1$). Also σ_3:$S_v < 1$ where σ_3
692 calculated from LOT data is observed for 13 tests conducted at depth intervals anywhere
693 from ≈102 to 3611 m TVD in northern and central HSM boreholes (Table 1), and from 3
694 tests at depth intervals of ≈ 357-1586 m TVD in southern HSM boreholes (Table 1). Several
695 factors can result in localized normal faulting regime at subduction margins including 1)
696 uncertainties in calculated UCS values and/or σ_3 magnitudes used to determine stress states
697 in this study, 2) the presence of local, active normal faults, and 3) fluctuations in stress
698 magnitudes modulated by seismic cycles.

699 ### 5.2.1. Uncertainties in calculated UCS values and σ_3 magnitudes

700 Estimations of S_{Hmax} magnitudes are highly sensitive to the UCS values used, particularly
701 when UCS is determined from empirical relationships not constrained by laboratory testing
702 (Zoback, 2007). Due to lack of direct UCS data in this region, and a lack of empirical
703 relationships for the formations of this region to determine UCS from other rock properties,

this study relied on the use or a range of empirical relationships developed elsewhere to generate a low and high limit for UCS at the HSM. These UCS ranges were then used to generate the lowest and highest limits of S_{Hmax} magnitude. When the lowest limit of UCS is used it can result in a potentially extensional stress state such that $S_{hmin} \approx S_{Hmax} \leq S_v$. As such, the uncertainty in calculated UCS values, and the resulting potential errors it can introduce into a stress model for the HSM, highlight the importance of dedicated laboratory tests for developing robust empirical relationships for UCS in the HSM region, and subduction regions like this, where stress is a critical geological consideration for hazard and resource management.

Inaccuracy involved in LOT measurements (section 3.3) along with the lack of detail reported on LOT results introduces an unknown level of uncertainty on estimated σ_3 magnitudes, and hence on estimated σ_3:S_v ratios using this data. Additionally, lack of LOT data along each borehole necessitates the estimation of σ_3 profiles from the average σ_3:S_v = 0.95, which also carries uncertainty. As a result, we recognize the potential impact this has on calculations of S_{Hmax} magnitudes here, as well as on any interpretations of regional stress state and tectonics. To investigate the potential effect of σ_3 uncertainties on S_{Hmax} calculations, we use both the lower and upper limits of σ_3 values calculated from σ_3:S_v = 0.92-1, BO widths, and the lower and upper boundary of UCS values. This analysis reveals that the σ_3 magnitude uncertainties at the scale explored here have little influence on S_{Hmax} magnitude calculations ($\pm$3.5 Mpa) and hence do not change our findings about the stress regime and tectonics within the HSM (blue areas in Figure 3; Figure 7b,c; Figure 9a,b).

5.2.2 Presence of active normal faults

Extensional structures are common within the overriding plate of many subduction margins (Loveless et al., 2010; Moore et al., 2013). Normal faults in subduction zones are often attributed to gravitational instabilities associated with subduction erosions and subsidence, density imbalances produced by forearc uplifts, strain releases during earthquake cycles, and flexural rigidity of the subduction interface (Barnes & Nicol, 2004; Collot et al., 1996; Loveless et al., 2005; Park et al., 2002; Sacks et al., 2013). Within the HSM, localized extensional stresses within the overriding plate are suggested to result from processes such as slab rollback, forearc rotation (Nicol et al., 2007; Wallace et al., 2004), subduction erosion and related subsidence, gravitational collapse due to forearc uplift, and growth of bending-

735 moment faults (Barnes & Nicol, 2004; Chanier et al., 1999; Upton et al., 2003; Walcott,
736 1987; Wallace, Fagereng, et al., 2012).

737 The σ_3 magnitude of 8.4 MPa measured from LOP in borehole Tuhara-1/1A (590.8 m TVD;
738 Table 1) is lower than σ_3 values of 8.95 MPa estimated from normal faulting failure with a
739 friction coefficient of 0.6 (Equation 7). This lower σ_3 magnitude may indicate there are active
740 normal faults at this depth along this borehole. In addition, borehole Tuhara-1A is located
741 within the Tuhara anticline structure, formed by contractional stresses resulting from two
742 blind thrust faults beneath the structure (Western Energy New Zealand, 1999). Our stress
743 magnitudes and HRT's (2000) analysis suggests that the Tuhara structure currently
744 experiences a dominant strike-slip faulting regime ($S_{hmin} \leq S_v \leq S_{Hmax}$; $1 \leq A_\phi \leq 2$) along the
745 majority of the borehole, interspersed with intervals of normal faulting regime ($S_{hmin} \leq S_{Hmax}$
746 $\leq S_v$; $0 \leq A_\phi < 1$) mainly within the 1700-1820 m and 2100-2145 m TVD depth interval
747 (Figure 3). A prominent feature of the Tuhara structure, as indicated by seismic reflection
748 profiles, is observation of relatively short steep east- and west-dipping normal faults
749 throughout Pliocene and Miocene successions (Western Energy New Zealand, 1999; Barnes
750 et al., 2002). Accordingly, we relate the appearance of normal stress states in our data to the
751 normal structures that develop as part of the larger compressional structural architecture of
752 this borehole site, and not due to the previously discussed uncertainties in the calculated UCS
753 and/or σ_3 magnitude values. This could particularly be the case where both the calculated
754 lower and upper limit of S_{Hmax} magnitudes are less than S_V (for example at 1700-1820 mTVD
755 in Tuhara-1A; Figure 3).

756 **5.2.3. Stress field fluctuations modulated by seismic cycling**

757 Fluctuations in stress magnitudes can be caused by seismic cycling. It has been reported that
758 earthquake events generate stress drops of 0.01 to 100 MPa, depending on the rheology,
759 roughness of fault, geometry of slip area, and heterogeneous stress fields (Allmann &
760 Shearer, 2009; Baltay et al., 2011; Candela et al., 2011; Cocco et al., 2016; Oth et al., 2010).
761 The observation of localized normal faulting regimes in the HSM may be related to seismic
762 cycling in the region. The normal faulting regimes observed along central HSM boreholes
763 Kauhauroa-2 (1980-2075 m TVD), Kauhauroa-5 (1330-1345 m TVD), and Tuhara-1A (1700-
764 1820 m TVD) occur where S_{Hmax} and S_v are very similar and are greater than S_{hmin} (Figure 3,
765 Figure 7b & 7c). In such stress state scenarios, a post-seismic stress drop of only a few MPa
766 after great earthquakes or frequent moderate earthquakes in the HSM region could perturb the

delicately balanced stress magnitudes surrounding these boreholes, switching $\sigma_1 = S_{Hmax}$ to $\sigma_1 = S_v$ i.e. from a reverse/strike-slip to a normal stress state, accompanied by small rotations in the S_{Hmax} orientation.

6 Conclusions

This work represents the first comprehensive determination of the *in-situ* stress state of the HSM margin using available borehole data. We found a $\sigma_3:S_v$ = 0.6-1 at depths above 650-700 m TVD, while $\sigma_3:S_v$ = 0.92-1 below this depth interval along the HSM. Stress magnitudes calculated from borehole data indicate that the $S_{Hmax}:S_v$ ratios ranging from 0.95-1.81 in the central HSM and 0.95-3.12 in the the southern HSM. These principal stress magnitude results indicate a $\sigma_1 = S_{Hmax}$ and a thrust to strike-slip faulting regime across the both central and southern HSM. The pre-existing NNE/NE striking reverse faults along the both central and southern HSM infer that stress regime was initially in a contractional state such that $\sigma_3: S_v = 1$, $\sigma_1 = S_{Hmax}$, and a dominant NW-SE S_{Hmax}, consistent with NW-SE component of Pacific-Australian plate motion. Taking contemporary stress state of $\sigma_1 = S_{Hmax}$ and ENE-WSW S_{Hmax} orientation and initial stress state into account in the central HSM, these observations suggest that the compressional regime has shifted from subparallel to perpendicular to the NW-SE Hikurangi convergence direction overtime in this region. Variation of the central HSM stress state overtime may result from forces arising from Hikurangi forearc rotation either by itself or facilitated by the upper plate, shallow, high overpressures in the central HSM. Along-strike variation in slip behavior may also play a role by releasing stress overtime due to SSEs and frequent earthquakes, hence changing the stress state in the central HSM, while in the southern HSM, the modern WNW-ESE/ NW-SE σ_1 (S_{Hmax}) remains subparallel to NW-SE Hikurangi convergence direction overtime, may reflect the interseismic locked nature of the plate interface. Finally, stress determination highlights localized normal stress states within the HSM forearc interpreted to be due to processes such as the presence of localized active normal faults or fluctuations in stress magnitudes modulated by seismic cycles. The determination of HSM *in-situ* stresses in this study will provide an invaluable tool for improving our understanding of the stability of upper plate faults and will facilitate more quantitative efforts to assess the seismic hazard potential of the HSM that will support of disaster risk reduction plans.

Acknowledgments

This publication has emanated from research conducted with the financial support of Science Foundation Ireland (SFI) under Grant Number 17/RC-PhD/3481 and co funded by Geological survey of Ireland (GSI). The authors would like to thank the New Zealand Petroleum and Minerals group (NZPM) within the Ministry for Business, Innovation and Employment (MBIE) for providing access to borehole data and supporting materials for this study. We also thank Schlumberger for providing academic licenses for Techlog 2018.1 to University College Dublin and University of Liverpool. We thank MathWorks for providing academic licenses for MATLAB to University College Dublin. We thank Esri for providing the academic license of ArcGIS Pro to University College Dublin. For the purpose of Open Access, the author has applied a CC BY public copyright license to any Author Accepted Manuscript version arising from this submission.

Data Availability Statement

This research used data provided by the New Zealand Petroleum and Minerals group (NZPM) within the Ministry for Business, Innovation and Employment (MBIE). The borehole image logs used in this paper can accessed through MBIE's online free database (https://data.nzpam.govt.nz/GOLD/system/mainframe.asp). Borehole breakout measurements presented in this study can be accessed at https://github.com/BehboudiEffatGeo/StressCharacterization_HSM.git and https://doi.org/10.5281/zenodo. 7450966.

References

Aadnoy, B. S. (1990). Inversion technique to determine the in-situ stress field from fracturing data. *Journal of Petroleum Science and Engineering*, *4*(2), 127–141.

Addis, M. A., Hanssen, T. H., Yassir, N., Willoughby, D. R., & Enever, J. (1998). A Comparison Of Leak-Off Test And Extended Leak-Off Test Data For Stress Estimation. In *SPE/ISRM Rock Mechanics in Petroleum Engineering* (p. SPE-47235-MS). https://doi.org/10.2118/47235-MS

Allmann, B. P., & Shearer, P. M. (2009). Global variations of stress drop for moderate to large earthquakes. *Journal of Geophysical Research: Solid Earth*, *114*(B01310). https://doi.org/10.1029/2008JB005821

Ando, R., Takeda, N., & Yamashita, T. (2012). Propagation dynamics of seismic and aseismic slip governed by fault heterogeneity and Newtonian rheology. *Journal of Geophysical Research B: Solid Earth*, *117*(B11308). https://doi.org/10.1029/2012JB009532

Audet, P., Bostock, M. G., Christensen, N. I., & Peacock, S. M. (2009). Seismic evidence for overpressured subducted oceanic crust and megathrust fault sealing. *Nature*, *457*(7225), 76–78. https://doi.org/10.1038/nature07650

Baltay, A., Ide, S., Prieto, G., & Beroza, G. (2011). Variability in earthquake stress drop and apparent stress. *Geophysical Research Letters*, *38*(6). https://doi.org/10.1029/2011GL046698

Barnes, P. M., Lamarche, G., Bialas, J., Henrys, S., Pecher, I., Netzeband, G. L., Greinert, J., Mountjoy, J. J., Pedley, K., & Crutchley, G. (2010). Tectonic and geological framework for gas hydrates and cold seeps on the Hikurangi subduction margin , New Zealand. *Marine Geology*, *272*(1–4), 26–48. https://doi.org/10.1016/j.margeo.2009.03.012

Barnes, P. M., Lpinay, M. De, Collot, J. Y., Delteil, J., & Audru, J.-C. (1998). Strain partitioning in the transition area between oblique subduction and continental collision , Hikurangi margin ,. *Tectonics*, *17*(4), 534–557.

Barnes, P. M., & Nicol, A. (2004). Formation of an active thrust triangle zone associated with structural inversion in a subduction setting, eastern New Zealand. *Tectonics*, *23*(1), 1–25. https://doi.org/10.1029/2002TC001449

Barton, C. A., Zoback, M. D., & Burns, K. L. (1988). In-situ stress orientation and magnitude at the Fenton Geothermal Site, New Mexico, determined from wellbore breakouts. *Geophysical Research Letters*, *15*(5), 467–470.

Bassett, D., Sutherland, R., & Henrys, S. (2014). Slow wavespeeds and fluid overpressure in a region of shallow geodetic locking and slow slip, Hikurangi subduction margin, New Zealand. *Earth and Planetary Science Letters*, *389*, 1–13. https://doi.org/10.1016/j.epsl.2013.12.021

Beanland, S., & Haines, J. (1998). The kinematics of active deformation in the North Island, New Zealand, determined from geological strain rates. *New Zealand Journal of Geology and Geophysics*, *41*(4), 311–323. https://doi.org/10.1080/00288306.1998.9514813

Beavan, J., Tregoning, P., Bevis, M., Kato, T., & Meertens, C. (2002). Motion and rigidity of the Pacific Plate and implications for plate boundary deformation. *Journal of Geophysical Research: Solid Earth*, *107*(B10), ETG 19-1-ETG 19-15. https://doi.org/10.1029/2001jb000282

Beetham, R. D., McSaveney, M. J., & Read, S. A. L. (2018). Four extremely large landslides in New Zealand. In *Landslides* (pp. 97–102). Routledge.

Behboudi, E., Mcnamara, D. D., Lokmer, I., Wallace, L. M., & Saffer, D. M. (2022). Spatial Variation of Shallow Stress Orientation Along the Hikurangi Subduction Margin : Insights From In-Situ Borehole Image Logging Journal of Geophysical Research : Solid Earth. *Journal of Geophysical Research : Solid Earth*, *127*. https://doi.org/10.1029/2021JB023641

Bell, J. S. (1996). Petro Geoscience 1. In situ stresses in sedimentary rocks (part 1): measurement techniques. *Geoscience Canada*.

Bell, J. S. (2003). Practical methods for estimating in situ stresses for borehole stability applications in sedimentary basins. *Journal of Petroleum Science and Engineering*, *38*(3–4), 111–119. https://doi.org/10.1016/S0920-4105(03)00025-1

Bell, J. S., & Gough, D. I. (1979). Northeast-southwest compressive stress in Alberta evidence from oil wells. *Earth and Planetary Science Letters*, *45*(2), 475–482. https://doi.org/10.1016/0012-821X(79)90146-8

Brodsky, E. E., Mori, J. J., Anderson, L., Chester, F. M., Conin, M., Dunham, E. M., Eguchi, N., Fulton, P. M., Hino, R., Hirose, T., Ikari, M. J., Saffer, D. M., Saito, S., Sample, J., Sun, T., Toczko, S., & Ujiie, K. (2020). The State of Stress on the Fault Before , During , and After a Major Earthquake. *Annual Review of Earth and Planetary Sciences*, *48*(May). https://doi.org/10.1146/annurev-earth-053018-060507

Brodsky, E. E., Saffer, D., Fulton, P., Chester, F., Conin, M., Huffman, K., Moore, J. C., & Wu, H.-Y. (2017). The postearthquake stress state on the Tohoku megathrust as constrained by reanalysis of the JFAST breakout data. *Geophysical Research Letters*, *44*, 8294–8302. https://doi.org/10.1002/2017GL074027

Brudy, M., & Zoback, M. D. (1999). Drilling-induced tensile wall-fractures: implications for determination of in-situ stress orientation and magnitude. *International Journal of Rock*

Mechanics and Mining Sciences, *36*(2), 191–215.
Burgreen-Chan, B., Meisling, K. E., & Graham, S. (2016). Seismic reflection character of the Hikurangi subduction interface, New Zealand, in the region of repeated Gisborne slow slip events. *Basin Research*, *28*(4), 536–567. https://doi.org/10.1111/bre.12121
Candela, T., Renard, F., Bouchon, M., Schmittbuhl, J., & Brodsky, E. E. (2011). Stress Drop during Earthquakes: Effect of Fault Roughness Scaling. *Bulletin of the Seismological Society of America*, *101*(5), 2369–2387. https://doi.org/10.1785/0120100298
Chang, C., McNeill, L. C., Moore, J. C., Lin, W., Conin, M., & Yamada, Y. (2010). In situ stress state in the Nankai accretionary wedge estimated from borehole wall failures. *Geochemistry, Geophysics, Geosystems*, *11*(12), 1–17. https://doi.org/10.1029/2010GC003261
Chang, C., Zoback, M. D., & Khaksar, A. (2006). Empirical relations between rock strength and physical properties in sedimentary rocks. *Journal of Petroleum Science and Engineering*, *51*(3–4), 223–237. https://doi.org/10.1016/j.petrol.2006.01.003
Chanier, F., Ferriere, J., & Angelier, J. (1999). Extensional deformation across an active margin, relations with subsidence, uplift, and rotations: The Hikurangi subduction, New Zealand. *Tectonics*, *18*(5), 862–876.
Cocco, M., Tinti, E., & Cirella, A. (2016). On the scale dependence of earthquake stress drop. *Journal of Seismology*, *20*(4), 1151–1170. https://doi.org/10.1007/s10950-016-9594-4
Collot, J. Y., Delteil, J., Lewis, K. B., Davy, B., Lamarche, G., Audru, J. C., Barnes, P., Chanier, F., Chaumillon, E., Lallemand, S., De Lepinay, B. M., Orpin, A., Pelletier, B., Sosson, M., Toussaint, B., & Uruski, C. (1996). From oblique subduction to intra-continental transpression: Structures of the southern Kermadec-Hikurangi margin from multibeam bathymetry, side-scan sonar and seismic reflection. *Marine Geophysical Research*, *18*(2–4), 357–381. https://doi.org/10.1007/BF00286085
Couzens-Schultz, B. A., & Chan, A. W. (2010). Stress determination in active thrust belts: An alternative leak-off pressure interpretation. *Journal of Structural Geology*, *32*(8), 1061–1069. https://doi.org/10.1016/j.jsg.2010.06.013
Darby, D., & Ellis, S. (2001). Evaluating Overpressure in Compressional Regimes Using Geomechanical Modeling. *PESA Eastern Australian Basins Symposium*, 613–620.
Darby, D., & Funnell, R. H. (2001). Overpressure associated with a convergent plate margin: East Coast Basin, New Zealand. *Petroleum Geoscience*, *7*(3), 291–299. https://doi.org/10.1144/petgeo.7.3.291
Darby, David, & Funnell, R. H. (2001). Overpressure associated with a convergent plate margin : East Coast Basin , New Zealand. *Petroleum Geoscience*, *7*(3), 291–299. https://doi.org/Mcnamara, D. D., Behboudi, E., Wallace, L., Saffer, D., Cook, A. E., & Fagereng, A. (2021). Variable In Situ Stress Orientations Across the Northern Hikurangi Subduction Margin Geophysical Research Letters. Petroleum Geoscience, 7(3), 291–299. https://doi.org/https://doi.org/10.1144/petgeo.7.3.291
Davy, B. (1992). The influence of subducting plate buoyancy on subduction of the Hikurangi-Chatham Plateau beneath the North Island, New Zealand. In *Geology and geophysics of continental margins*.
Davy, B., Hoernle, K., & Werner, R. (2008). Hikurangi Plateau: Crustal structure, rifted formation, and Gondwana subduction history. *Geochemistry, Geophysics, Geosystems*, *9*(7). https://doi.org/10.1029/2007GC001855
Delvaux, D., Moeys, R., Stapel, G., Petit, C., Levi, K., Miroshnichenko, A., Ruzhich, V., & San, V. (1997). Paleostress reconstructions and geodynamics of the Baikal region , Central Asia , Part 2 . Cenozoic rifting. *Tectonophysics*, *282*(1–4), 1–38.
Dixon, T. H., Jiang, Y., Malservisi, R., McCaffrey, R., Voss, N., Protti, M., & Gonzalez, V. (2014). Earthquake and tsunami forecasts: Relation of slow slip events to subsequent

earthquake rupture. *Proceedings of the National Academy of Sciences of the United States of America*, *111*(48), 17039–17044. https://doi.org/10.1073/pnas.1412299111

Doser, D. I., & Webb, T. H. (2003). Source parameters of large historical (1917-1961) earthquakes, North Island, New Zealand. *Geophysical Journal International*, *152*, 795–832. https://doi.org/10.1046/j.1365-246X.2003.01895.x

Downes, G. L. (2006). The 1904 Ms6.8 Mw7.0-7.2 Cape Turnagain, New Zealand, earthquake. *Bulletin of the New Zealand Society for Earthquake Engineering*, *39*(4), 183–207. https://doi.org/10.5459/bnzsee.39.4.183-207

Dutta, N. C., Bachrach, R., & Mukerji, T. (2021). *Quantitative Analysis of Geopressure for Geoscientists and Engineers*. Cambridge University Press. https://doi.org/10.1017/9781108151726

Eberhart-Phillips, D., Bannister, S., & Reyners, M. (2017). Deciphering the 3-D distribution of fluid along the shallow Hikurangi subduction zone using P- and S-wave attenuation. *Geophysical Journal International*, *211*(2), 1032–1045. https://doi.org/10.1093/gji/ggx348

Evanzia, D., Wilson, T., Savage, M. K., & Hamish, H. (2017). Stress Orientations in a Locked Subduction Zone at the Southern Hikurangi Margin, New Zealand. *Journal of Geophysical Research : Solid Earth*, *122*, 7895–7911. https://doi.org/10.1002/2017JB013998

Fagereng, A., & Ellis, S. (2009). On factors controlling the depth of interseismic coupling on the Hikurangi subduction interface, New Zealand. *Earth and Planetary Science Letters*, *278*, 120–130. https://doi.org/10.1016/j.epsl.2008.11.033

Gao, H., Schmidt, D. A., & Weldon, R. J. (2012). Scaling relationships of source parameters for slow slip events. *Bulletin of the Seismological Society of America*, *102*(1), 352–360. https://doi.org/10.1785/0120110096

Gardner, G. H. F., Gardner, L. W., & Gregory, A. (1974). Formation velocity and density—The diagnostic basics for stratigraphic traps. *Geophysics*, *39*(6), 770–780.

Grapes, R., & Downes, G. (1997). The 1855 Wairarapa, New Zealand, earthquake. *Bulletin of the New Zealand Society for Earthquake Engineering*, *30*(4), 271–368. https://doi.org/10.5459/bnzsee.30.4.271-368

Griffin, A. G. (2019). Subsurface SHMAX determined from a borehole image log, onshore southern East Coast Basin, New Zealand. *New Zealand Journal of Geology and Geophysics*, *62*(2), 273–290. https://doi.org/10.1080/00288306.2019.1570946

Griffin, A. G., Bland, K. J., Morgans, H. E. G., Strogen, D. P., Griffin, A. G., Bland, K. J., Morgans, H. E. G., Strogen, D. P., Bland, K. J., Morgans, H. E. G., & Strogen, D. P. (2021). A multifaceted study of the offshore Titihaoa-1 drillhole and a Neogene accretionary slope basin , Hikurangi subduction margin. *New Zealand Journal of Geology and Geophysics*, *0*(0), 1–26. https://doi.org/10.1080/00288306.2021.1932527

Gunter, J. M., & Moore, C. V. (1986). Improved Use of Wireline Testers for Reservoir Evaluation. In *International Meeting on Petroleum Engineering* (p. SPE-14063-MS). https://doi.org/10.2118/14063-MS

Hardebeck, J. L. (2012). *Coseismic and postseismic stress rotations due to great subduction zone earthquakes*. *39*(October), 1–6. https://doi.org/10.1029/2012GL053438

Hardebeck, J. L., & Okada, T. (2018). Temporal Stress Changes Caused by Earthquakes: A Review. *Journal of Geophysical Research : Solid Earth*, *123*, 1350–1365. https://doi.org/10.1002/2017JB014617

Heidbach, O., Rajabi, M., Cui, X., Fuchs, K., Müller, B., Reinecker, J., Reiter, K., Tingay, M., Wenzel, F., Xie, F., Ziegler, M. O., Zoback, M. Lou, & Zoback, M. (2018). The World Stress Map database release 2016: Crustal stress pattern across scales. *Tectonophysics*, *744*(July), 484–498. https://doi.org/10.1016/j.tecto.2018.07.007

Heise, W., Ogawa, Y., Bertrand, E. A., Caldwell, T. G., Yoshimura, R., Ichihara, H., Bennie, S. L., Seki, K., Saito, Z., Matsunaga, Y., Suzuki, A., Kishita, T., & Kinoshita, Y. (2019). Electrical resistivity imaging of the inter-plate coupling transition at the Hikurangi subduction margin, New Zealand. *Earth and Planetary Science Letters*, *524*, 115710. https://doi.org/10.1016/j.epsl.2019.115710

Huffman, K. A., & Saffer, D. M. (2016). In situ stress magnitudes at the toe of the Nankai Trough Accretionary Prism, offshore Shikoku Island, Japan. *Journal of Geophysical Research : Solid Earth*, *121*, 1202–1217. https://doi.org/10.1002/2015JB012415

Ito, Y., & Obara, K. (2006). *Very low frequency earthquakes within accretionary prisms are very low stress-drop earthquakes*. *33*(January), 1–4. https://doi.org/10.1029/2006GL025883

Jaeger, J. C., Cook, N. G. W., & Zimmerman, R. (2009). *Fundamentals of rock mechanics*. John Wiley & Sons.

Kodaira, S., Iidaka, T., Kato, A., Park, J. O., Iwasaki, T., & Kaneda, Y. (2004). High pore fluid pressure may cause silent slip in the Nankai Trough. *Science*, *304*(5675), 1295–1298. https://doi.org/10.1126/science.1096535

Kurzawski, R. M., Niemeijer, A. R., Stipp, M., Charpentier, D., Behrmann, J. H., & Spiers, C. J. (2018). Frictional Properties of Subduction Input Sediments at an Erosive Convergent Continental Margin and Related Controls on Décollement Slip Modes: The Costa Rica Seismogenesis Project. *Journal of Geophysical Research: Solid Earth*, *123*(10), 8385–8408. https://doi.org/10.1029/2017JB015398

Lange, W. P. de, & Moon, V. G. (2004). Estimating earthquake and landslide tsunami hazard for the New Zealand coast. *Bulletin of the New Zealand Society for Earthquake Engineering*, *37*(2), 62–69. https://doi.org/10.5459/bnzsee.37.2.62-69

Langridge, R. M., Ries, W. F., Litchfield, N. J., Villamor, P., Dissen, R. J. Van, Barrell, D. J. A., Rattenbury, M. S., Heron, D. W., Haubrock, S., Townsend, D. B., Lee, J. M., Berryman, K. R., Nicol, A., Cox, S. C., & Stirling, M. W. (2016). The New Zealand Active Faults Database. *New Zealand Journal of Geology and Geophysics ISSN:*, *59*(1), 86–96. https://doi.org/10.1080/00288306.2015.1112818

Lawrence, M. J. F. (2018). Structural and Sedimentological Interpretation of Well Data from the Wairoa Area , North Island , New Zealand. *GNS Science Report 2018/28*, *August*, 1–76. https://doi.org/10.21420/G23W81

Lee, J., Swarbrick, R., & Connor, S. O. (2022). Kicks and their significance in pore pressure prediction. *Petroleum Geoscience*, *28*. https://doi.org/10.1144/petgeo2021-061

Litchfield, N. J., Van Dissen, R., Sutherland, R., Barnes, P. M., Cox, S. C., Norris, R., Beavan, R. J., Langridge, R., Villamor, P., Berryman, K., Stirling, M., Nicol, A., Nodder, S., Lamarche, G., Barrell, D. J. A., Pettinga, J. R., Little, T., Pondard, N., Mountjoy, J. J., & Clark, K. (2014). A model of active faulting in New Zealand. *New Zealand Journal of Geology and Geophysics*, *57*(1), 32–56. https://doi.org/10.1080/00288306.2013.854256

Liu, Y., & Rice, J. R. (2007). Spontaneous and triggered aseismic deformation transients in a subduction fault model. *Journal of Geophysical Research*, *112*(B09404). https://doi.org/10.1029/2007JB004930

Loveless, J. P., Allmendinger, R. W., Pritchard, M. E., & González, G. (2010). Normal and reverse faulting driven by the subduction zone earthquake cycle in the northern Chilean fore arc. *Tectonics*, *29*(TC2001). https://doi.org/10.1029/2009TC002465

Loveless, J. P., Hoke, G. D., Allmendinger, R. W., González, G., Isacks, B. L., & Carrizo, D. A. (2005). Pervasive cracking of the northern Chilean Coastal Cordillera: New evidence for forearc extension. *Geology*, *33*(12), 973–976. https://doi.org/10.1130/G22004.1

Ltd., I.-P. E. (NZ). (2002). *Waingaromia-2 Well Completion Report*. Ministry of Economic

Development New Zealand, Unpublished Open file Petroleum Report 2767.
Ma, K. F., Chan, C. H., & Stein, R. S. (2005). Response of seismicity to Coulomb stress triggers and shadows of the 1999 Mw=7.6 Chi-Chi, Taiwan, earthquake. *Journal of Geophysical Research: Solid Earth*, *110*(B05S19). https://doi.org/10.1029/2004JB003389
Ma, Y. Z., & Holditch, S. A. (2015). Unconventional Oil and Gas Resources Handbook: Evaluation and Development. In *Unconventional Oil and Gas Resources Handbook: Evaluation and Development*. Gulf professional publishing. https://doi.org/10.1016/C2014-0-01377-9
Mantovani, E., Viti, M., Albarello, D., Tamburelli, C., Babbucci, D., & Cenni, N. (2000). Role of kinematically induced horizontal forces in Mediterranean tectonics: insights from numerical modeling. *Journal of Geodynamics*, *30*(3), 287–320. https://doi.org/10.1016/S0264-3707(99)00067-8
Marotta, A. ., Bayer, U., Thybo, H., & Scheck, M. (2002). Origin of the regional stress in the North German basin: results from numerical modelling. *Tectonophysics*, *360*(1–4), 245–264. https://doi.org/10.1016/S0040-1951(02)00358-X
Mcnamara, D. D., Behboudi, E., Wallace, L., Saffer, D., Cook, A. E., & Fagereng, A. (2021). Variable In Situ Stress Orientations Across the Northern Hikurangi Subduction Margin Geophysical Research Letters. *Geophysical Research Letters*, *48*. https://doi.org/https://doi. org/10.1029/2020GL091707
McNamara, D. D., Behboudi, E., Wallace, L., Saffer, D., Cook, A. E., Fagereng, A., Paganoni, M., Wu, H. Y., Kim, G., Lee, H., Savage, H. M., Barnes, P., Pecher, I., LeVay, L. J., & Petronotis, K. E. (2021). Variable In Situ Stress Orientations Across the Northern Hikurangi Subduction Margin. *Geophysical Research Letters*, *48*(5). https://doi.org/10.1029/2020GL091707
Moore, G. F., Boston, B. B., Sacks, A. F., & Saffer, D. M. (2013). Analysis of normal fault populations in the Kumano Forearc Basin , Nankai Trough , Japan : 1 . Multiple orientations and generations of faults from 3-D coherency mapping. *Geochemistry, Geophysics, Geosystems*, *114*, 1989–2002. https://doi.org/10.1002/ggge.20119
Moos, D., & Zoback, M. D. (1990). Utilization of observations of well bore failure to constrain the orientation and magnitude of crustal stresses: application to continental, Deep Sea Drilling Project, and Ocean Drilling Program boreholes. *Journal of Geophysical Research*, *95*(B6), 9305–9325. https://doi.org/10.1029/JB095iB06p09305
Mountjoy, J. J., & Barnes, P. M. (2011). Active upper plate thrust faulting in regions of low plate interface coupling, repeated slow slip events, and coastal uplift: Example from the Hikurangi Margin, New Zealand. *Geochemistry, Geophysics, Geosystems*, *12*(1), 1–26. https://doi.org/10.1029/2010GC003326
Nicol, A., & Beavan, J. (2003). Shortening of an overriding plate and its implications for slip on a subduction thrust, central Hikurangi Margin, New Zealand. *Tectonics*, *22*(6), n/a-n/a. https://doi.org/10.1029/2003tc001521
Nicol, A., Mazengarb, C., Chanier, F., Rait, G., Uruski, C., & Wallace, L. (2007). Tectonic evolution of the active Hikurangi subduction margin, New Zealand, since the Oligocene. *Tectonics*, *26*(4), 1–24. https://doi.org/10.1029/2006TC002090
Oth, A., Bindi, D., Parolai, S., & Di Giacomo, D. (2010). Earthquake scaling characteristics and the scale-(in)dependence of seismic energy-to-moment ratio: Insights from KiK-net data in Japan. *Geophysical Research Letters*, *37*(19). https://doi.org/10.1029/2010GL044572
Park, J.-O., Tsuru, T., Kodaira, S., Cummins, P. R., & Kaneda, Y. (2002). Splay Fault Branching Along the Nankai Subduction Zone. *Science*, *297*(5584), 1157–1160. https://doi.org/10.1126/science.1074111

Pedley, K. L., Barnes, P. M., Pettinga, J. R., & Lewis, K. B. (2010). Seafloor structural geomorphic evolution of the accretionary frontal wedge in response to seamount subduction, Poverty Indentation, New Zealand. *Marine Geology*, *270*(1–4), 119–138. https://doi.org/10.1016/j.margeo.2009.11.006

Power, W. L., Reyners, M., & Wallace, L. M. (2008). Tsunami hazard posed by earthquakes on the Hikurangi subduction zone interface. In *GNS Science Consultancy Report 2008/40* (Issue May).

Reiter, K. (2021). Stress rotation – The impact and interaction of rock stiffness and faults. *Solid Earth*, *12*(6), 1287–1307. https://doi.org/10.5194/se-12-1287-2021

Riedel, M., Malinverno, A., Wang, K., Goldberg, D., & Guerin, G. (2016). Horizontal compressive stress regime on the northern Cascadia margin inferred from borehole breakouts. *Geochemistry, Geophysics, Geosystems*, *17*(9), 3529–3545. https://doi.org/10.1002/2016GC006443

Sacks, A., Saffer, D. M., & Fisher, D. (2013). Analysis of normal fault populations in the Kumano forearc basin, Nankai Trough, Japan: 2. Principal axes of stress and strain from inversion of fault orientations. *Geochemistry, Geophysics, Geosystems*, *14*(6), 1973–1988. https://doi.org/10.1002/ggge.20118

Saffer, D. M., & Wallace, L. M. (2015). The frictional, hydrologic, metamorphic and thermal habitat of shallow slow earthquakes. *Nature Publishing Group*, *8*. https://doi.org/10.1038/ngeo2490

Schellart, W. P., & Rawlinson, N. (2013). Global correlations between maximum magnitudes of subduction zone interface thrust earthquakes and physical parameters of subduction zones. *Physics of the Earth and Planetary Interiors*, *225*, 41–67. https://doi.org/10.1016/j.pepi.2013.10.001

Seeber, L., & Armbruster, J. G. (2000). Earthquakes as beacons of stress change. *Nature*, *407*(6800), 69–72. https://doi.org/10.1038/35024055

Sibson, R. H. (1974). Frictional constraints on thrust, wrench and normal faults. *Nature*, *249*(5457), 542–544.

Stein, R. S. (1999). The role of stress transfer in earthquake occurrence. *Nature*, *402*(December), 605–609.

Townend, J., Sherburn, S., Arnold, R., Boese, C., & Woods, L. (2012). Three-dimensional variations in present-day tectonic stress along the Australia-Pacific plate boundary in New Zealand. *Earth and Planetary Science Letters*, *353–354*, 47–59. https://doi.org/10.1016/j.epsl.2012.08.003

Ujiie, K., & Kimura, G. (2014). Earthquake faulting in subduction zones: insights from fault rocks in accretionary prisms. *Progress in Earth and Planetary Science*, *1*(7). https://doi.org/10.1186/2197-4284-1-7

Upton, P., Koons, P. O., & Eberhart-phillips, D. (2003). Extension and partitioning in an oblique subduction zone , New Zealand : Constraints from three-dimensional numerical modeling. *Tectonics*, *22*(6). https://doi.org/10.1029/2002TC001431

Van Ruth, P. J., Hillis, R. R., & Swarbrick, R. E. (2002). Detecting overpressure using porosity-based techniques in the Carnarvon basin, Australia. *The APPEA Journal*, *42*(1), 559–569.

Vavrycuk, V. (2015). Earthquake Mechanisms and Stress Field. In *Encyclopedia of Earthquake Engineering* (Issue January 2015). https://doi.org/10.1007/978-3-642-36197-5

Vernik, L., & Zoback, M. D. (1992). Estimation of maximum horizontal principal stress magnitude from stress-induced well bore breakouts in the Cajon Pass scientific research borehole. *Journal of Geophysical Research: Solid Earth*, *97*(B4), 5109–5119.

Walcott, R. I. (1987). Geodetic Strain and the Deformational History of the North Island of

New Zealand during the Late Cainozoic Author (s): R . I . Walcott Source : Philosophical Transactions of the Royal Society of London . Series A , Mathematical Published by : Royal Soci. *Philosophical Transactions of the Royal Society of London. Series A, Mathematical and Physical Sciences*, *321*(1557), 163–181. https://www.jstor.org/stable/37727

Wallace, L. M. (2020). Slow Slip Events in New Zealand. *Annual Review of Earth and Planetary Sciences*, *48*, 175–203. https://doi.org/10.1146/annurev-earth-071719- 055104

Wallace, L. M., & Beavan, J. (2010). Diverse slow slip behavior at the Hikurangi subduction margin, New Zealand. *Journal of Geophysical Research: Solid Earth*, *115*(12), 1–20. https://doi.org/10.1029/2010JB007717

Wallace, L. M., Beavan, J., Bannister, S., & Williams, C. (2012). Simultaneous long-term and short-term slow slip events at the Hikurangi subduction margin, New Zealand: Implications for processes that control slow slip event occurrence, duration, and migration. *Journal of Geophysical Research B: Solid Earth*, *117*(B11402). https://doi.org/10.1029/2012JB009489

Wallace, L. M., Beavan, J., McCaffrey, R., & Darby, D. (2004). Subduction zone coupling and tectonic block rotations in the North Island, New Zealand. In *Journal of Geophysical Research: Solid Earth* (Vol. 109, Issue 12, pp. 1–21). https://doi.org/10.1029/2004JB003241

Wallace, L. M., & Eberhart-Phillips, D. (2013). *Newly observed , deep slow slip events at the central Hikurangi margin , New Zealand : Implications for downdip variability of slow slip and tremor , and relationship to seismic structure*. *40*, 5393–5398. https://doi.org/10.1002/2013GL057682

Wallace, L. M., Fagereng, Å., & Ellis, S. (2012). Upper plate tectonic stress state may infl uence interseismic coupling on subduction megathrusts. *Geology*, *40*(10), 895–898. https://doi.org/10.1130/G33373.1

Wallace, L. M., Reyners, M., Cochran, U., Bannister, S., Barnes, P. M., Berryman, K., Downes, G., Eberhart-Phillips, D., Fagereng, A., Ellis, S., Nicol, A., McCaffrey, R., Beavan, R. J., Henrys, S., Sutherland, R., Barker, D. H. N., Litchfield, N., Townend, J., Robinson, R., … Power, W. (2009). Characterizing the seismogenic zone of a major plate boundary subduction thrust: Hikurangi Margin, New Zealand. *Geochemistry, Geophysics, Geosystems*, *10*(10). https://doi.org/10.1029/2009GC002610

Webb, T. H., & Anderson, H. (1998). Focal mechanisms of large earthquakes in the North Island of New Zealand: slip partitioning at an oblique active margin. *Geophysical Journal International*, *134*, 40–86. https://doi.org/10.1046/j.1365-246x.1998.00531.x

White, A. J., Traugott, M. O., & Swarbrick, R. E. (2002). The use of leak-o ff tests as means of predicting minimum in-situ stress. *Petroleum Geoscience*, *8*, 189–193. https://doi.org/https://doi.org/10.1144/petgeo.8.2.189

Wu, H., Chan, C., Shiraishi, K., Wspanialy, A., & Sugihara, T. (2019). Observed stress state for the IODP Site C0002 and implication to the stress fi eld of the Nankai Trough subduction zone. *Tectonophysics*, *765*(April), 1–10. https://doi.org/10.1016/j.tecto.2019.04.017

Zhang, J., & Yin, S. (2017). *Real-Time Pore Pressure Detection : Indicators and Improved Methods*. *2017*(1).

Zoback, M. D. (2007). *Reservoir Geomechanics*. Cambridge University Press.

Zoback, M. D., Barton, C. A., Brudy, M., Castillo, D. A., Finkbeiner, T., Grollimund, B. R., Moos, D. B., Peska, P., Ward, C. D., & Wiprut, D. J. (2003). Determination of stress orientation and magnitude in deep wells. *International Journal of Rock Mechanics and Mining Sciences*, *40*(7–8), 1049–1076. https://doi.org/10.1016/j.ijrmms.2003.07.001

Indo-Pacific Energy (NZ) Ltd. (2002). Waingaromia-2 Well Completion Report, Ministry of Economic Development New Zealand, Unpublished Open file Petroleum Report 2767.
Tap Oil Limited. (2004). Tawatawa-1 Well Completion Report, Ministry of Economic Development New Zealand, Unpublished Open file Petroleum Report 3067.
Western Energy New Zealand. (1999), Tuhara-1A Well Completion Report, PEP 38329, Ministry of Economic Development New Zealand, Unpublished Open file Petroleum Report 2470.
Western Energy New Zealand. (2001), Well Completion Report Kauhauroa-4B, Ministry of Economic Development New Zealand, Unpublished Open file Petroleum Report 2610.

Figure 1.

(a)

(b)

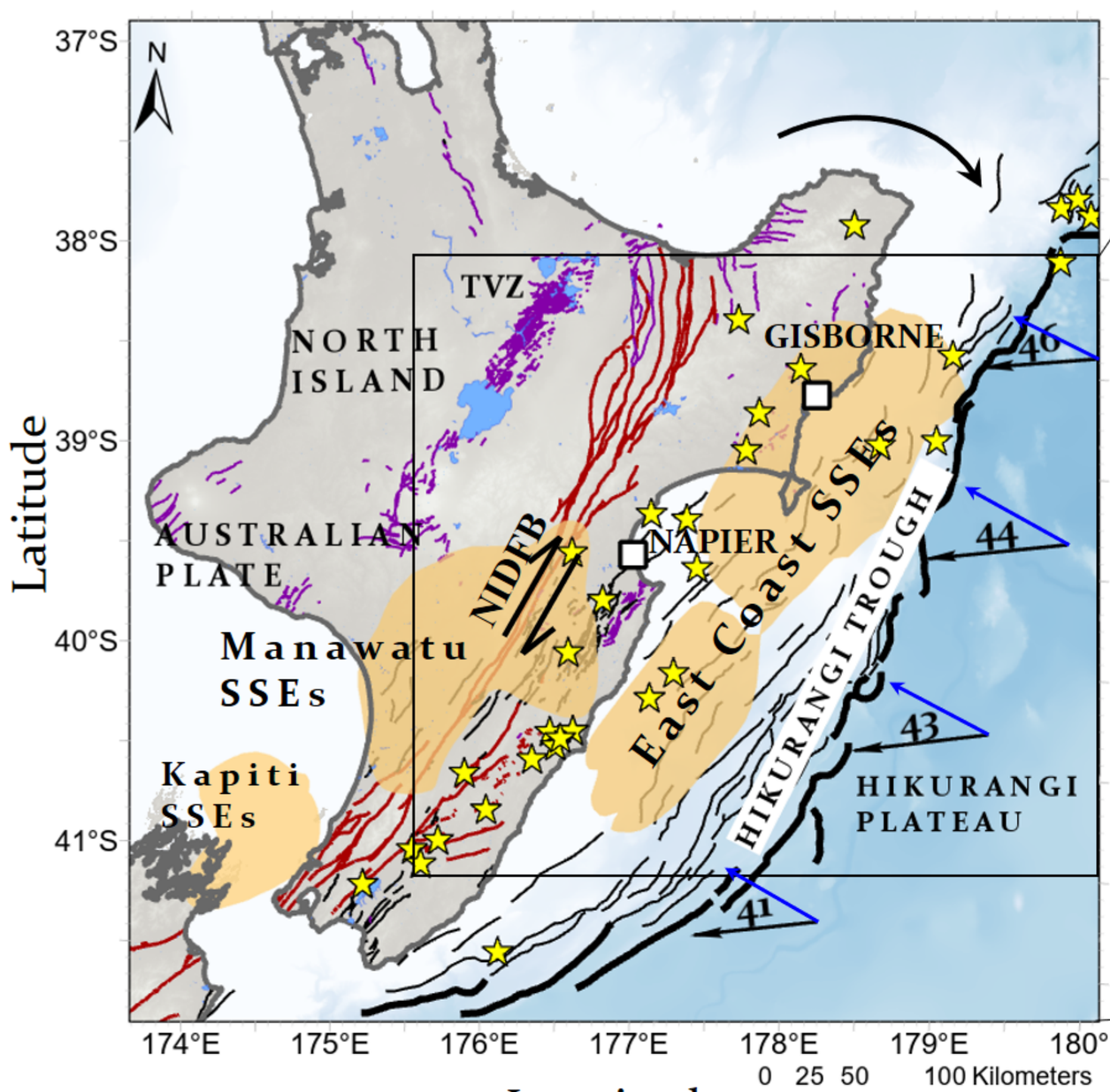

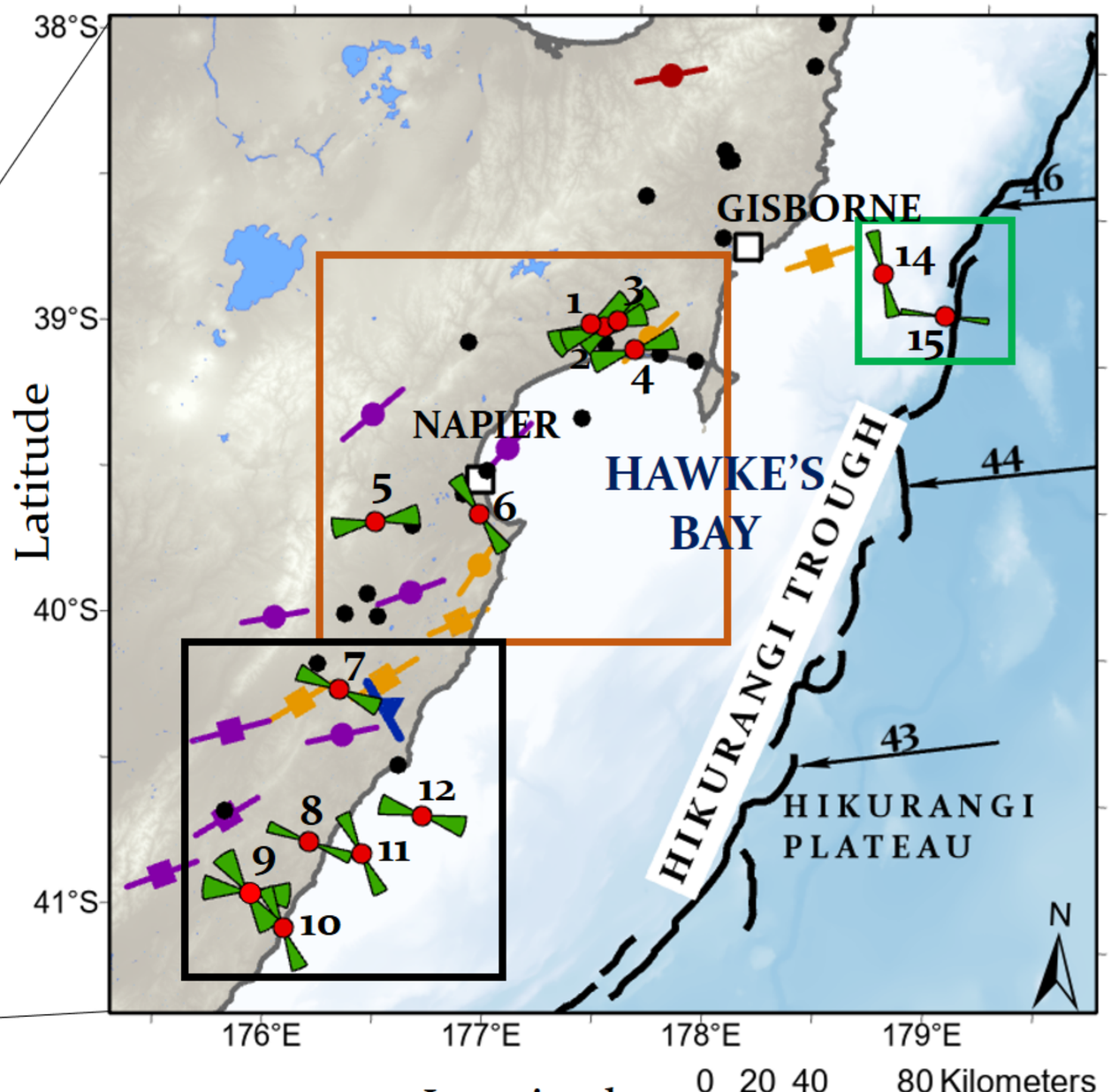

Historical earthquakes

Pacific-Australian plate motion

Normal component of Pacific-Australian plate motion

Forearc rotation direction

Reverse fault

Strike-slip fault

Normal fault

S_{Hmax} from image logs and four-arm calliper logs

Depth (km)

0
15
30
45
60

S_{Hmax} orientation from focal mechanisms

Normal faulting regime

Strike-slip faulting regime

Thrust faulting regime

≥50 mm total SSE slip (2002 - 2012)

East Coast boreholes

Boreholes with S_{Hmax} orientation:

1: Makareo-1
2: Kauhauroa-2
3: Kauhauroa-5
4: Tuhara-1A
5: Kereru -1
6: Whakatu-1
7: Ngapaeruru-1
8: Te Mai-2
9: Ranui-2
10: Orui-1A
11: Titihaoa-1
12: Tawatawa-1
13: U1519A
14: U1518B

Northern HSM-IODP sites

Central HSM

Southern HSM

Figure 2.

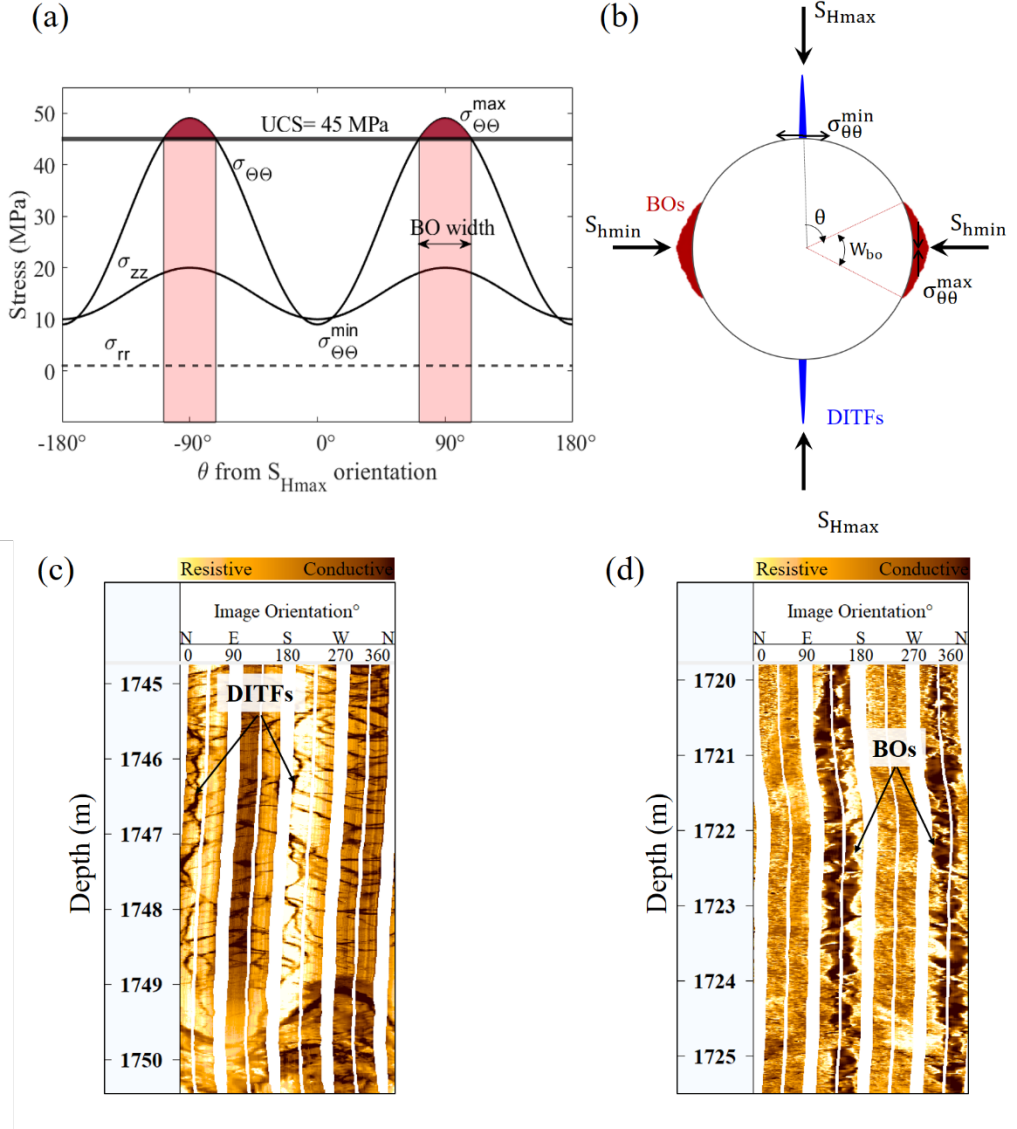
(a)
UCS= 45 MPa
$\sigma^{max}_{\theta\theta}$
$\sigma_{\theta\theta}$
BO width
σ_{zz}
σ_{rr}
$\sigma^{min}_{\theta\theta}$
Stress (MPa)
50
40
30
20
10
0
-180°
-90°
0°
90°
180°
θ from S_{Hmax} orientation
(b)
S_{Hmax}
$\sigma^{min}_{\theta\theta}$
BOs
S_{hmin}
θ
W_{bo}
S_{hmin}
$\sigma^{max}_{\theta\theta}$
DITFs
S_{Hmax}
(c)
Resistive
Conductive
Image Orientation°
N E S W N
0 90 180 270 360
DITFs
Depth (m)
1745
1746
1747
1748
1749
1750
(d)
Resistive
Conductive
Image Orientation°
N E S W N
0 90 180 270 360
BOs
Depth (m)
1720
1721
1722
1723
1724
1725

Figure 3.

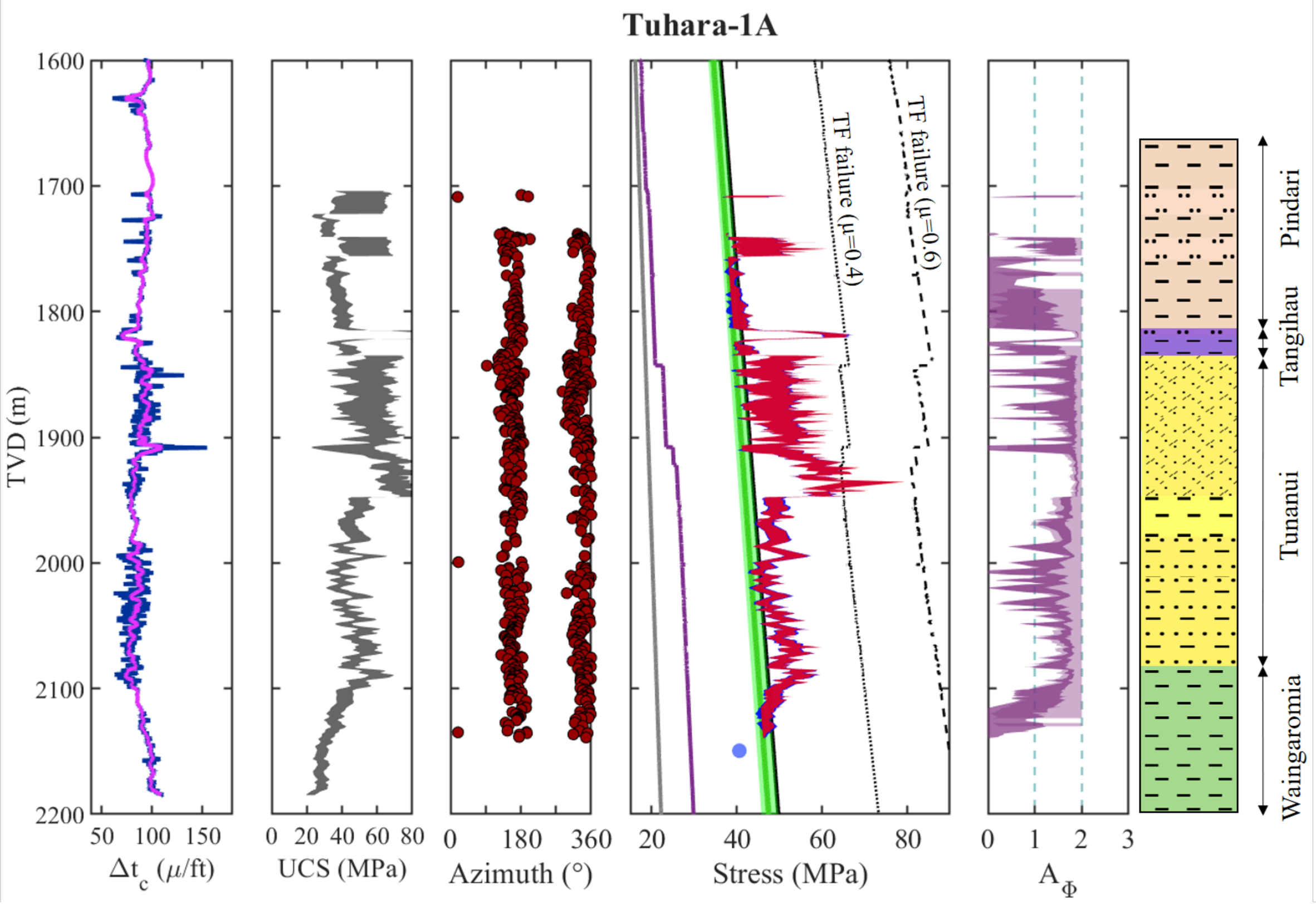
Tuhara-1A
TVD (m)
1600
1700
1800
1900
2000
2100
2200
50 100 150
Δt_c (μ/ft)
0 20 40 60 80
UCS (MPa)
0 180 360
Azimuth (°)
20 40 60 80
Stress (MPa)
0 1 2 3
A_Φ
TF failure (μ=0.4)
TF failure (μ=0.6)
Pindari
Tangihau
Tunanui
Waingaromia

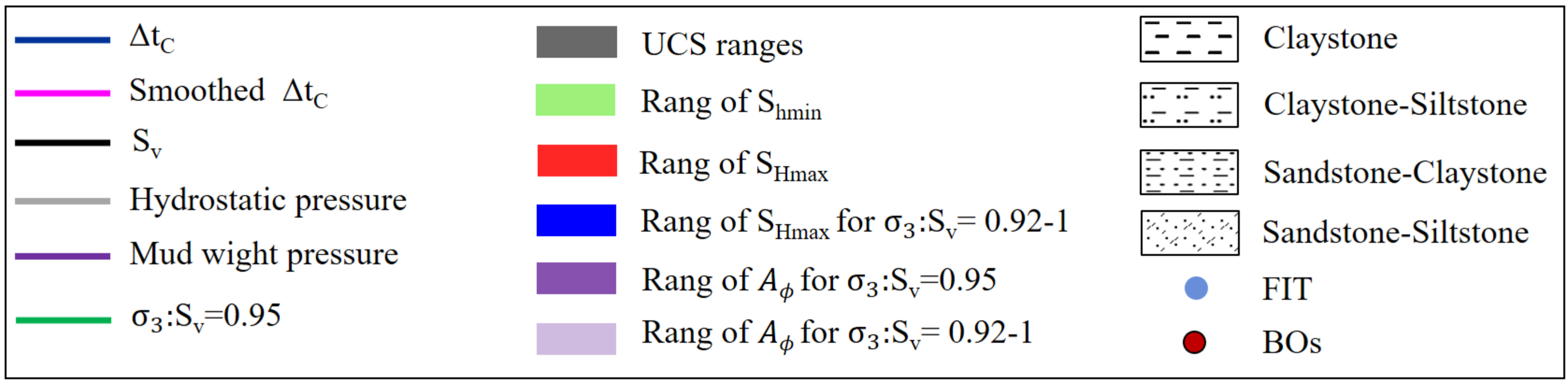
Δt_C
Smoothed Δt_C
S_v
Hydrostatic pressure
Mud wight pressure
σ_3:S_v=0.95
UCS ranges
Rang of S_hmin
Rang of S_Hmax
Rang of S_Hmax for σ_3:S_v= 0.92-1
Rang of A_ϕ for σ_3:S_v=0.95
Rang of A_ϕ for σ_3:S_v= 0.92-1
Claystone
Claystone-Siltstone
Sandstone-Claystone
Sandstone-Siltstone
FIT
BOs

Figure 4.

Onshore

Offshore

TVD

Pressure (MPa)

26.97 MPa/km

22.58 MPa/km

20.92 MPa/km

S_v data from Northern & Central HSM's boreholess

S_v data from Southern HSM's boreholes

Hydrostatic pressure

Average S_v gradient

Lower and upper S_v gradient

Figure 5.

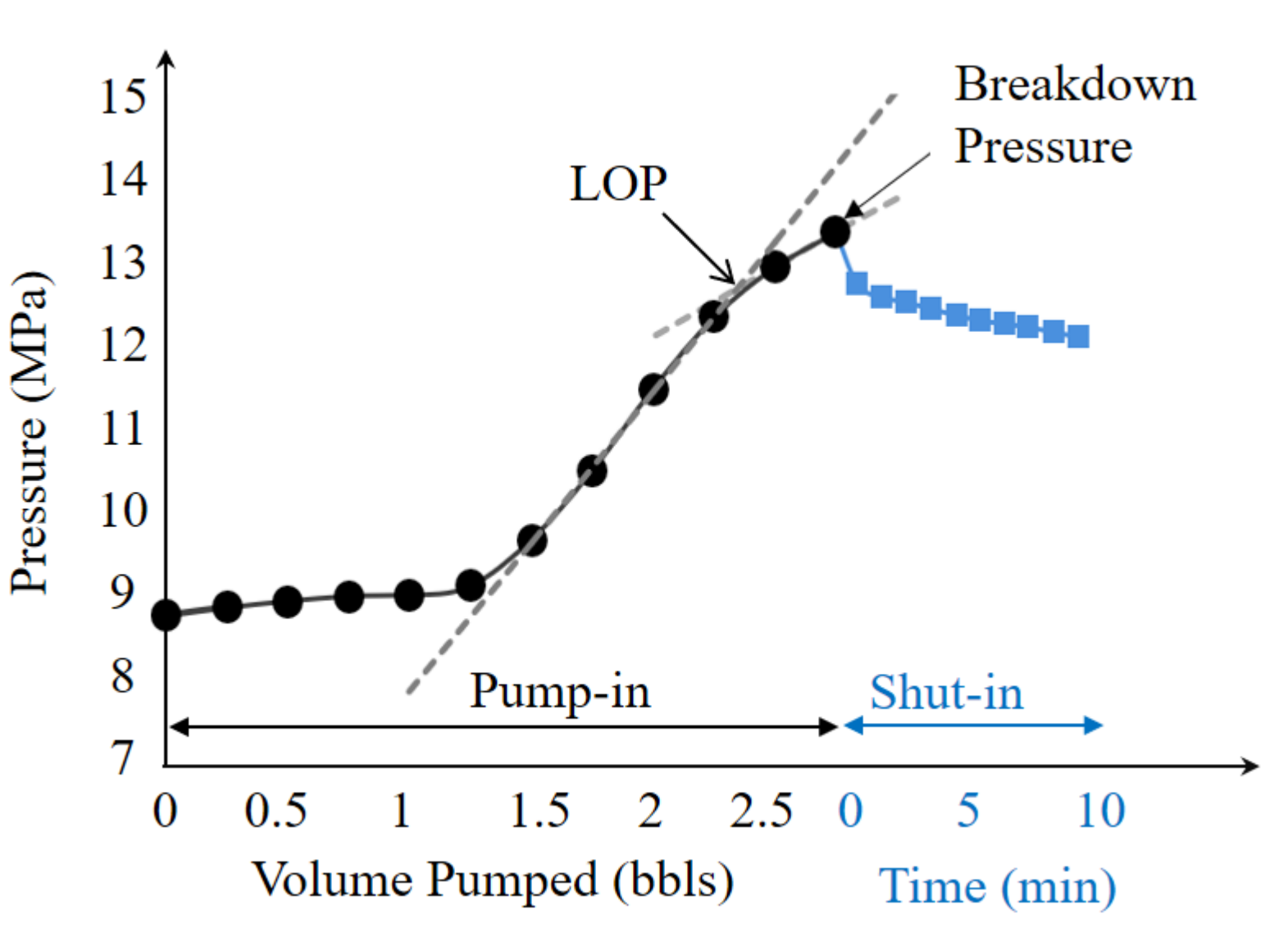
Breakdown
Pressure
LOP
Pump-in
Shut-in
Pressure (MPa)
15
14
13
12
11
10
9
8
7
0
0.5
1
1.5
2
2.5
0
5
10
Volume Pumped (bbls)
Time (min)

6.

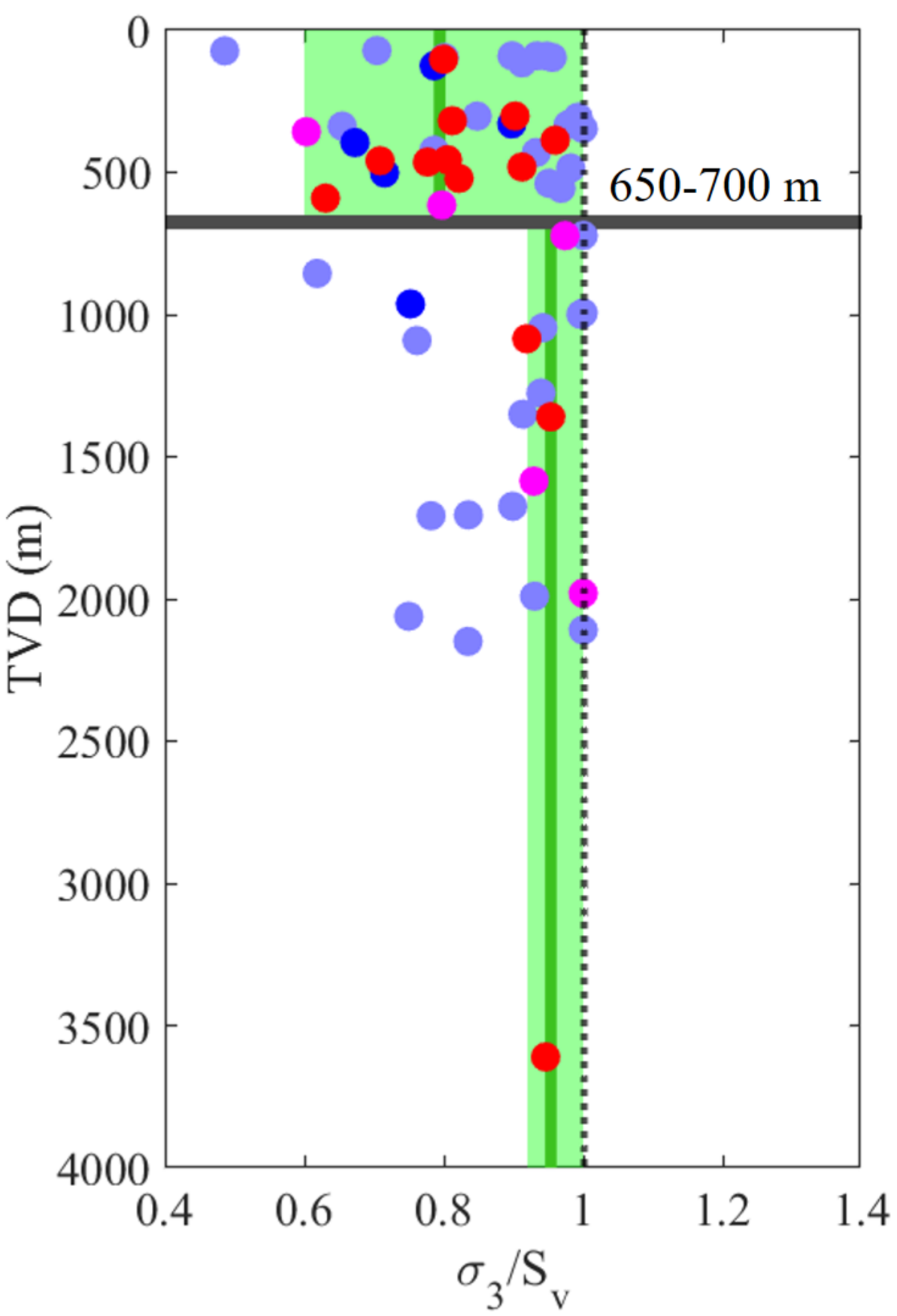
0
500
1000
1500
2000
2500
3000
3500
4000
TVD (m)
650-700 m
0.4
0.6
0.8
1
1.2
1.4
σ3/Sv

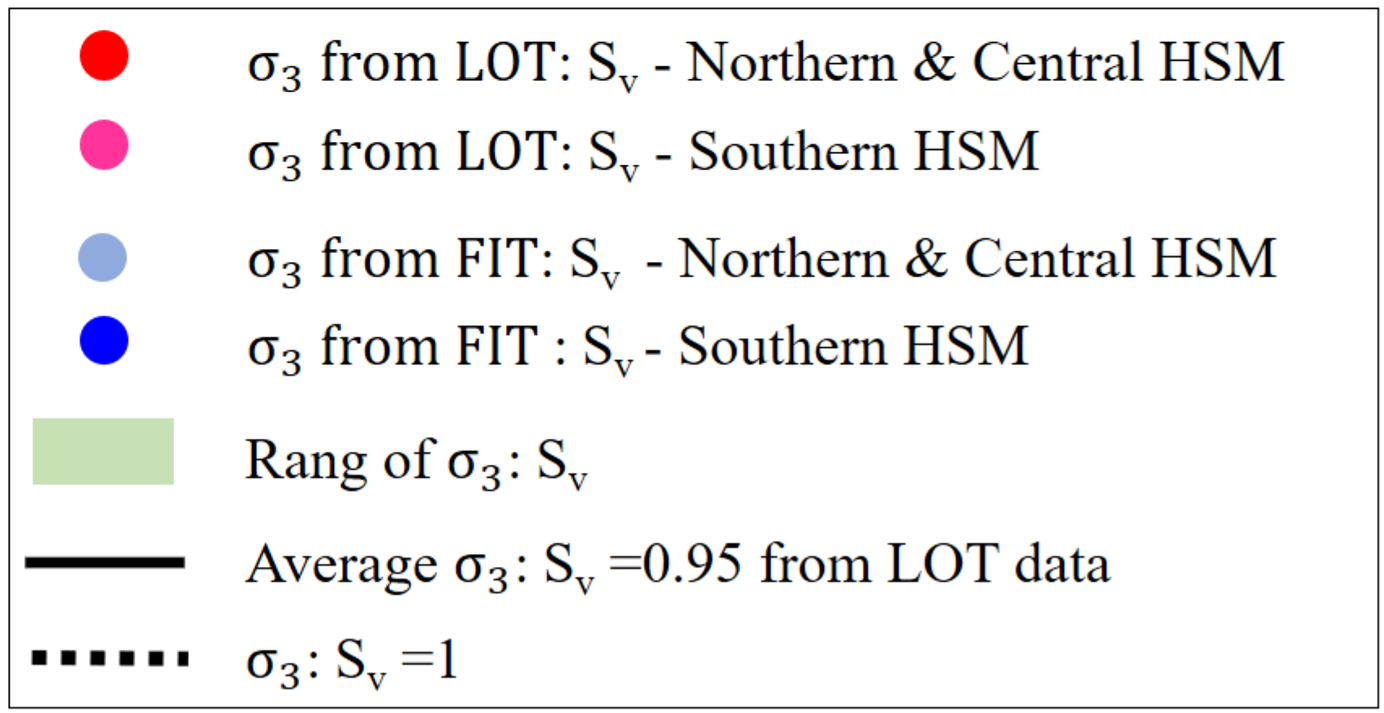
σ3 from LOT: Sv - Northern & Central HSM
σ3 from LOT: Sv - Southern HSM
σ3 from FIT: Sv - Northern & Central HSM
σ3 from FIT : Sv - Southern HSM
Rang of σ3: Sv
Average σ3: Sv =0.95 from LOT data
σ3: Sv =1

Figure 7.

(a)

Makareao-1

(b)

Kauhauroa-2

(c)

Kauhauroa-5

TVD (m)

Azimuth (°)

Stress (MPa)

A_Φ

BOs

DITFs

FIT

P_p from RFT

S_v

Mud wight pressure

Mud wight pressure calibrated with RFT

σ_3:S_v= 0.95

Rang of S_{hmin}

Rang of S_{Hmax}

Rang of S_{Hmax} for σ_3:S_v= 0.92-1

Rang of A_ϕ for σ_3:S_v=0.95

Rang of A_ϕ for σ_3:S_v= 0.92-1

Claystone-Siltstone

Siltstone

Claystone

Sandstone-Claystone

Sandstone-Siltstone

Limestone

Tuff

Pindari

Kauhauroa

Wheao

Weber

Tangihau

Tunanui

Waingaromia

Rere

TF failure (μ=0.4)

TF failure (μ=0.6)

Figure 8.

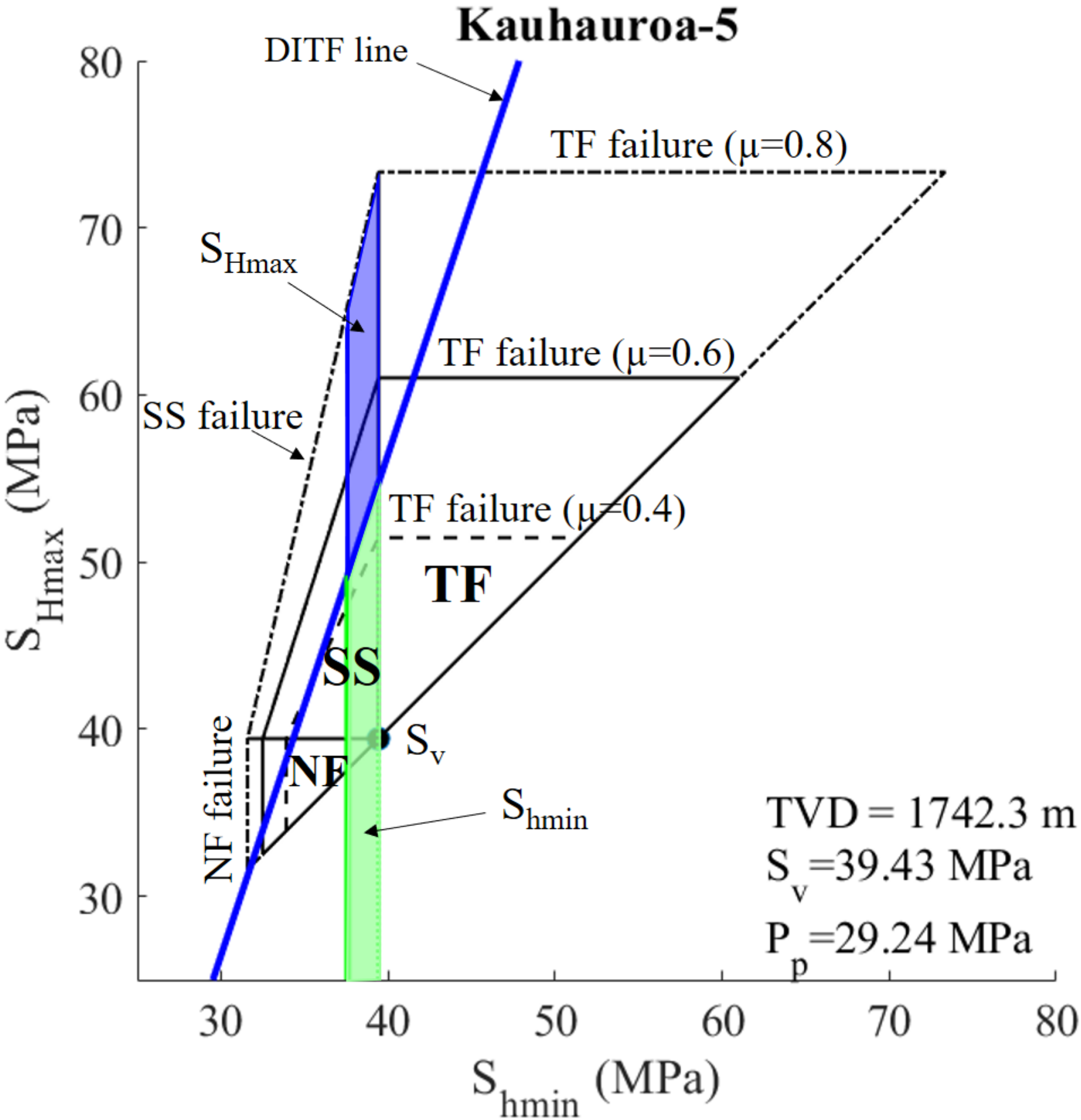
Kauhauroa-5
DITF line
TF failure (μ=0.8)
TF failure (μ=0.6)
TF failure (μ=0.4)
SS failure
NF failure
S_Hmax
S_hmin
S_v
TF
SS
NF
TVD = 1742.3 m
S_v =39.43 MPa
P_p =29.24 MPa
S_Hmax (MPa)
S_hmin (MPa)
80
70
60
50
40
30
30
40
50
60
70
80

Figure 9.

(a) Ngapaeruru-1

(b) Ranui-2

(c) Titihaoa-1

(d) Tawatawa-1

TVD (m)

Azimuth (°)

Stress (MPa)

A_Φ

BOs

DITFs

FIT

P_p from RFT

S_v

Mud wight pressure

Mud wight pressure calibrated with RFT

σ_3:S_v= 0.95

Rang of S_{hmin}

Rang of S_{Hmax}

Rang of S_{Hmax} for σ_3:S_v= 0.92-1

Rang of A_ϕ for σ_3:S_v=0.95

Rang of A_ϕ for σ_3:S_v= 0.92-1

Claystone

Siltstone

Claystone-Siltstone

Sandstone

Sandstone-Siltstone

Sandstone-Claystone

Limestone

TF failure (μ=0.4)

Whangai

Tangaruhe

Torlesse

Lower Kapitean

Tongaporutuan

Whakataki

Springhill

TF failure (μ=0.6)

Figure 10.

(a)

(b)

(c)

TVD (m)

500
1000
1500
2000
2500
3000

2000 3000 4000 5000 6000

V_p (m/s)

0 25 50 75 100

UCS (MPa)

0 10 20 30 40

Young's modulus (GPa)

Southern HSM

Ngapaeruru-1
Rauni-2
Tawatawa-1
Titihaoa-1

Central HSM

Kauhauroa-2
Kauhauroa-5
Makareo-1
Tuhara-1A

Waitahora-1